Crustal deformation in the northeastern Tibetan Plateau: the roles of northward indentation of the Qaidam basin and southward underthrusting of the North China Craton

Chuang Sun [1, 2, *], Zhigang Li [1, 2], Wenjun Zheng [1, 2], Dong Jia [3], Shuang Yang [3]

[1] Guangdong Provincial Key Lab of Geodynamics and Geohazards, School of Earth Sciences and Engineering, Sun Yat-sen University, Guangzhou 510275, China

[2] Southern Marine Science and Engineering Guangdong Laboratory, Zhuhai, China,

[3] School of Earth Sciences and Engineering, Nanjing University, Nanjing 210093, China

*Corresponding authors: Chuang Sun (sunchuang@mail.sysu.edu.cn and sunny_like@163.com)

Abstract

Northward indentation of the Qaidam Basin (QB) and southward underthrusting of North China Craton (NCC) lithospheric mantle beneath the Qilian Shan (QLS) are two frequently-cited geodynamic modes for interpreting the evolution of the northeastern Tibetan Plateau. We here aim at understanding the roles of these two dynamic processes in crustal deformation and how they interact during plateau growth in the NE margin by using sandbox experiments that simulate the convergence of the QB-QLS belt through indentation and underthrusting type of boundary conditions individually, alternately or synchronously. Results illustrate that 1) Underthrusting beneath the QLS favors a gently-tapering, one-sided thrust wedge only above the downgoing slab. 2)

Indentation of the QB promotes the occurrence of doubly vergent convergent belts with two oppositely-tapering thrust wedges spreading from the slab boundary. 3) Diverse convergence histories lead to distinct deformation patterns for the modelled convergent belts. However, only when indentation and underthrusting occurred synchronously, the modelled thrust wedge resembles current QB-QLS belt in terms of growth sequence, wedge geometry and deformation localization pattern, indicating that bidirectional compression mode maybe the best approximation for the late Cenozoic northeastern Tibetan Plateau. Our experiments further reveal that shift of boundary conditions like alternation of geodynamic drivers and encountered foreland buttress, would result in limited changes in uplift rate of individual structures. Instead, switch between different structural evolutionary stages causes more pronounced variations and should be noted when interpreting thermochronologic data from the northeastern Tibetan Plateau.

Key Points

1) Indentation of the Qaidam Basin promotes occurrence of the doubly vergent Qaidam-Qilian Shan thrust belt

2) Presence of underthrusting beneath the Qilian Shan belt could significantly lower the taper angle of overlying Qilian Shan wedge

3) Late Cenozoic Qaidam-Qilian Shan belt evolves under the framework of bidirectional compression

1 Introduction

Collision and subsequent continuous convergence between the Indian and Eurasian plates has driven the formation of the most magnificent highland on this planet, the Tibetan Plateau (Fielding et al., 1994; Clark and Royden, 2000, Figure 1). Without question, the northward motion of the Indian Plate dominates the geodynamic framework under which the current plateau is shaped (Yin and Harrison, 2000; Tappoinner et al., 2001; Zhang et al., 2004). However, some geophysical observations across the northeastern margin of the Tibetan Plateau, far into the continental interior, have revealed signs reflecting southward mantle underthrusting of the North China Craton (NCC), with the leading edge beneath the southern Qilian Shan (Gao R. et al., 1999; Feng et al., 2014; Ye Z. et al., 2015, Figure 2) or farther south (Kind et al., 2002; Zhao J. et al., 2010; Zhao W. et al., 2011). The crust and its underlying mantle should undergo synchronous shortening. If south-directed underthrusting of the NCC lithospheric mantle has occurred, a corresponding southward basal drag should also be exerted on the overlying crust. This situation would lead to totally different stress conditions and dynamic setting from the previous perspective that northward compression from the Himalayan belt forces indentation of the Qaidam Basin and dominates regional crustal deformation in the plateau's northeastern margin (Zhang et al., 2004; Gan et al., 2007; Clark, 2012; Cheng et al., 2015; Zheng et al., 2017).

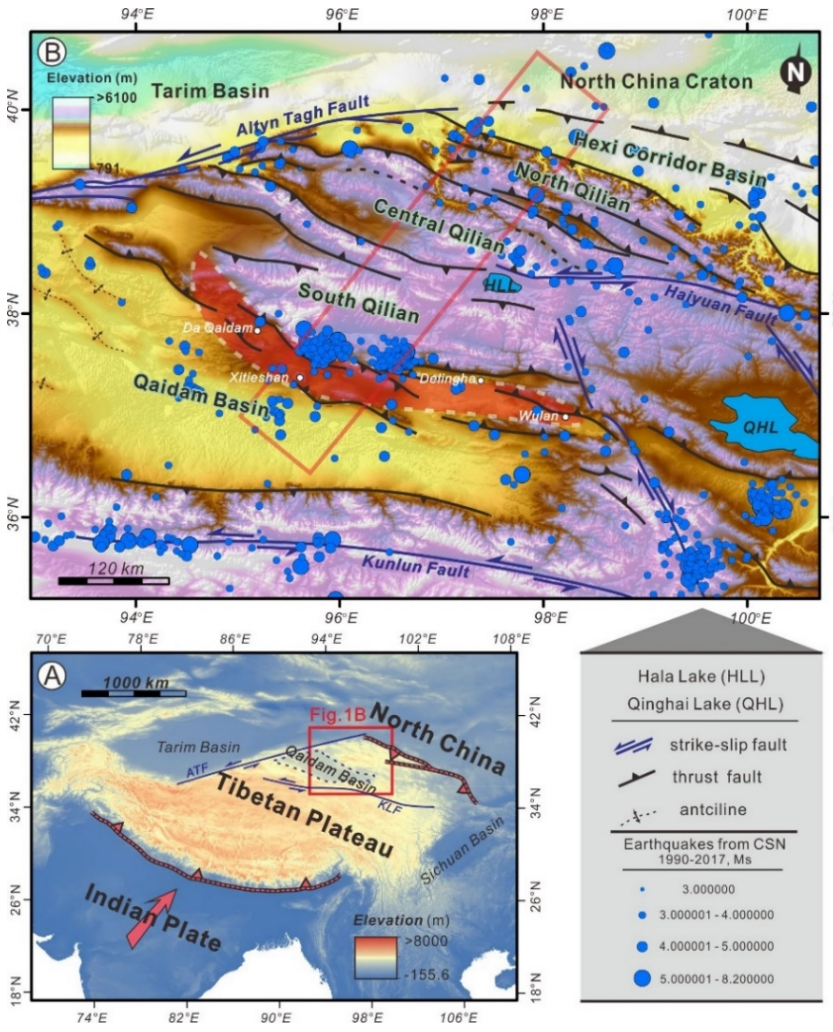

58

59 **Figure 1** (A) Topographical map of the Himalaya-Tibetan orogen showing the location of study
60 area. (B) Map-view structural configuration presented in west segment of modern Qaidam-Qilian
61 belt. Major faults are indicated, as well as the distribution of earthquakes (1990-2017 Ms≥3.0). The
62 data set is provided by China Earthquake Data Center (http://data.earthquake.cn). Area marked by
63 red ribbon is the north Qaidam ultra-high pressure metamorphic belt from Song et al. (2014).

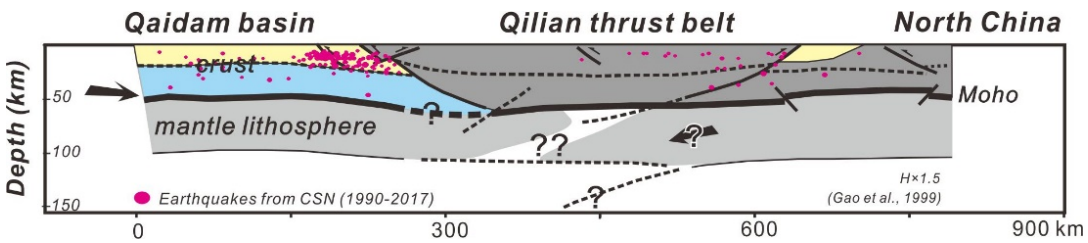

64

65 **Figure 2** Preliminary lithospheric structure of the Northeastern Tibetan Plateau (after the Golmud-
66 Ejin transect, Gao et al., 1999). The black bold lines represent Moho and dashed lines are feasible
67 detachment layers. The black arrows show regional compression. Yellow colors indicate basin
68 sedimentation. The pink dots are earthquakes (1990-2017 Ms≥3.0) within the red box in Figure 1B.

The southward underthrusting of the NCC is an important end member geodynamic model for the evolution of the (northeastern) Tibetan Plateau. Its related issues are still highly debated. First, several other geophysical observations covering the nearby region suggest that the southern edge of the NCC is located immediately beneath the Hexi Corridor Basin (Figure 1A), which argues against large-scale southward underthrusting (Liang et al., 2012; Shen X. et al., 2015, 2017; Wei et al., 2017). Assuming this process occurred, when this event started and what roles it played in the Cenozoic evolution of the northeastern Tibetan Plateau remain unclear. Only limited and indirect evidence has been obtained, which lead to some interesting inferences; for example, according to the high Cenozoic strain (>53%) focused in the northeastern Qilian Shan front and the regional strain rate-based shortening model they built, Zuza et al. (2016, 2019) suggested that the northeastern plateau evolved in a similar way to that of southern Tibet and southward underthrusting of the NCC may be in progress. They also inferred that this deep process initiated at ~20-15 Ma and was partly synchronized with the northward indentation of the Qaidam Basin, producing bidirectional compression (Gao et al., 1999; Shi et al., 2017; Zuza et al., 2019). In contrast, Allen et al. (2017) proposed a Palaeozoic age for this subduction on the basis of Precambrian signatures associated with the NCC that were observed from Palaeozoic plutons in the Qilian Shan. Consequently, they estimated much less crustal shortening (155-175 km) for the Cenozoic Qilian Shan, half to two-thirds of the amount proposed by Zuza et al. (2016, 2019). If the hypothesis of Allen et al. (2017) is true, underthrusting of the NCC may have provided only certain inherited structures for Cenozoic reactivation.

At this point, more detailed knowledge of crustal responses to different kinds of deep geodynamic processes (northward indentation versus southward underthrusting, as well as their temporal and spatial variations) would be indispensable. If the differences in the deformation sequence and style of the overlying crust could be identified and related to these deep processes, important constraints would be imposed on current disputes about how the NCC behaves during the formation of the modern northeastern Tibetan Plateau, as well as on our understanding of the Cenozoic evolution of the northeastern Tibetan Plateau itself.

Sandbox modelling is a powerful tool in simulating crustal deformation because it generates real localized deformation zones (faults) by using modelling materials that possess strain hardening and softening analogues to real rocks (e.g., Klinkmuller et al., 2016; Ritter et al., 2016; Reber et al., 2020). Moreover, its physical nature has great advantages in the ability to set complex velocity boundary conditions according to real deep geodynamics such as oblique convergence (McClay et al., 2004; Del Castello et al., 2005), reverses in subduction polarity (Del Castello et al., 2004, 2005) and convergence among multiple blocks (Malavieille and Trullenque, 2009; Sun M et al., 2018), which are particularly suitable for investigating the cases of spatio-temporal changes in geodynamic conditions likely in the Qaidam-Qilian Shan belt.

In this paper, we present five sandbox models that simulate the convergence between two blocks analogous to those proposed for the Qaidam-Qilian Shan belt in the northeastern Tibetan Plateau. Two end member basal velocity boundary conditions

(BVBCs) corresponding to northward indentation of the Qaidam Basin and southward underthrusting beneath the Qilian Shan are applied individually, alternately or synchronously to provide experimental convergence. With quantitative analysis of these sandbox models and comparison with nature, we attempt to identify possible diagnostic features for different deep geodynamic conditions and decipher the likely crustal responses of the northeastern Tibetan Plateau (Qaidam-Qilian region) to the underlying processes as well as their temporal variations.

2 Geological setting of the Qaidam-Qilian Shan belt in the northeastern Tibetan Plateau

The northeastern Tibetan Plateau is composed of the Qilian Shan belt in the north and the Qaidam Basin in the south (Figure 1). The Qilian Shan belt consists of several NW–SE-striking, thrust-controlled mountains with the highest elevation of >5000 m present in the south (Figure 3). The overall topographic relief of this belt is small, but a northward decrease in elevation is clearly observed. All faults beneath the high mountains are believed to merge into a low seismic velocity zone at mid-crustal depth, which shallows northward and constrains an orogenic wedge tapering northeast (Burchfiel et al., 1989; Tapponnier et al., 1990; Meyer et al., 1998; Métivier et al., 1998; Yin and Harrison, 2000; Yin et al., 2008a; Allen et al., 2017; Cheng et al., 2018). Notably, this low-velocity zone has a higher shear wave velocity than that required for allowing crustal flow (e.g., Gao et al., 1999; Ye et al., 2015). Therefore, it is generally accepted to behave merely as a detachment layer and to decouple the intensely

deformed upper crust from the mid-lower crust and mantle lithosphere (e.g., Yang Y. et al., 2012; Bao et al., 2013; Feng et al., 2014; Li H. et al., 2014).

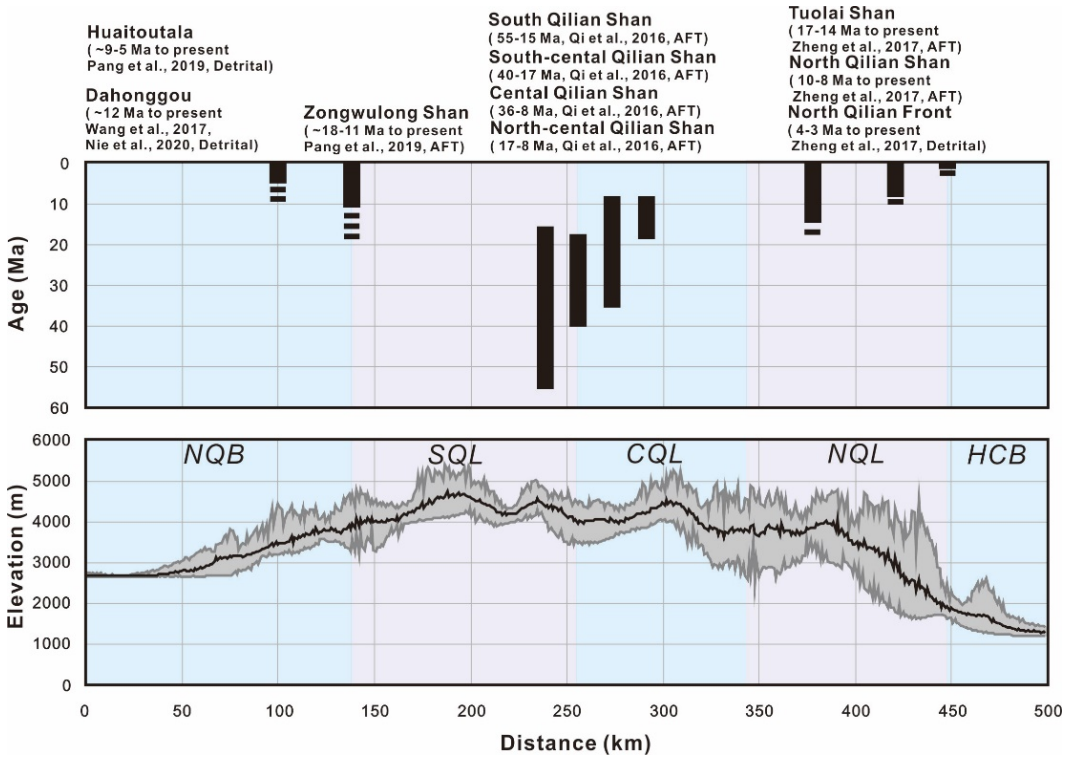

Figure 3 Mirror image relationship between the time of Cenozoic rapid exhumation and topographic relief across the study area. See the red box in Figure 1B for location of the swath profile. NQB: the Northeastern Qaidam Basin; SQL: the Southern Qilian Shan belt; CQL: the Central Qilian Shan belt; NQL: the Northeastern Qilian Shan belt; HCB: the Hexi Corridor Basin;

The Qaidam Basin, covering an area of ~120,000 km^2 between the Qilian Shan to the north and the Songpan-Ganzi in the south, is the largest intermontane basin within the Tibetan Plateau. As indicated by elastic thickness (Braitenberg et al., 2003), this basin has an exceptionally high strength, but significant upper crust deformation has taken place during the Cenozoic evolution, indicating that the present high strength should mainly rely on the deep crust and/or the mantle. The superficial structures within this basin are mainly characterized by small anticlines several kilometres wide. However,

as imaged by seismic profiles in the northeastern Qaidam Basin, a southward-tapering crustal wedge has developed at depth (Yin et al. 2002, 2008a, b). This wedge is controlled by the middle crustal detachment called the Main Qaidam detachment and involves a series of north-dipping thrusts in the crystalline basement. However, it is currently covered by thick sedimentary layers sourced from the adjacent south Qilian Shan.

Due to the lack of sufficient structural information from the highly elevated Qilian Shan belt, a solid structural cross-section covering the study area has not yet been constructed. However, the Qilian Shan belt and the northeastern Qaidam Basin clearly should be kinematically coupled. According to existing thermochronological and sedimentological studies, a progressive northward growth mode can be inferred, at least for the central-northeastern Qilian Shan belt, with rapid exhumation starting from the mid-late Miocene (17-14 Ma) in the Tuolai Shan, 10-8 Ma in the northeastern Qilian Shan and 4-3 Ma in front of the northeastern Qilian Shan (Zheng W. et al., 2013; Yuan et al., 2013; Zheng D et al., 2017; Hu X. et al., 2019; Pang J. et al., 2019; Yu J. et al., 2019, Figure 3). Near the northeastern margin of the Qaidam Basin, rapid cooling events since 11-18 Ma and 5-9 Ma have been detected and related to the initiation of thrusting in the southern Qilian Shan and the northeastern Qaidam Basin, respectively, almost synchronous with the northward deformation propagation in the central-northeastern Qilian Shan (Wang W. et al., 2017; Pang J. et al., 2019). In the southern Qilian Shan, the initiation of rapid Cenozoic uplift is still highly debated, specifically

regarding whether it took place at almost the same time as the collision between India and Eurasia (Jolivet et al., 2001; Qi B. et al., 2016; He et al., 2017, 2018; Lu et al., 2018) or significantly later than the collision, lagging 10-20 Ma or more (Wang W. et al., 2017; Nie et al., 2020). Additionally, the existence of a palaeo-Qilian Shan before the Cenozoic India-Asia collision has been proposed (Yin et al., 2008a; Zhang et al., 2017; Jian et al., 2018; Yu X. et al., 2019; Song et al., 2020), with pre-Cenozoic elevations up to ~2500 mm (Cheng et al., 2019). However, note that the above disputes do not hinder the understanding of first-order deformation styles in which the Qilian Shan belt and the northeastern Qaidam Basin compose a doubly vergent wedge that involves two back-to-back thrust belts that verge and expand in opposite directions, a structural style typically associated with collision zones (Koons, 1990; Willett et al., 1993; Beaumont et al., 1999; McClay and Whitehouse, 2004, Figure 4).

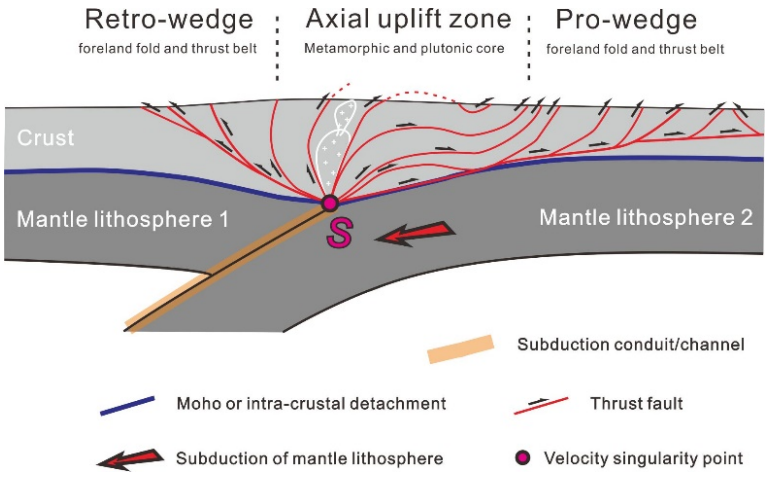

Figure 4 Conceptual model of continental subduction/underthrusting and the associated doubly vergent collisional orogenic wedge (Beaumont et al., 1999; McClay and Whitehouse, 2004). It should be noted that part of crustal materials may subduct with underlying mantle lithosphere.

3 Sandbox modelling

Whether and how the deformation sequence and features presented within the Qaidam-Qilian Shan belt relate to the underlying deep processes, such as southward underthrusting beneath the Qilian Shan belt and northward indentation of the Qaidam Basin, remain indistinct and are explored through sandbox modelling in the following.

3.1 Modelling strategy

Crustal deformation associated with terrane or continental collision and collage (formation of a doubly vergent orogenic wedge) can be simulated by imposing a singularity (S) point on the experimental base (Koon, 1990; Willett et al., 1993; Beaumont et al., 1999; McClay and Whitehouse, 2004, Figure 4). This base represents the plane where the (upper) crust detaches from the underlying mantle lithosphere. The S-point acts as a velocity singularity where one plate subducts beneath the other therefore is also the place where sequential crustal deformation roots and spreads laterally. Commonly, the setup of the S-point and the convergence of crustal layers may be implemented in two ways, 1) A subduction slot is created at the base of the sandbox and behaves as a fixed S-point. Modelling materials are transported towards the slot by an underlying conveyer (e.g., Storti et al., 2000; Del Castello et al., 2004; McClay and Whitehouse, 2004). 2) One or more rigid plates/blocks are used, with their edges behaving as fixed or mobile S-points (Stori et al., 2001; Soto et al., 2006; Malavieille and Trullenque, 2009; Sun M. et al., 2018). They can either drive the overlying

materials themselves to converge and deform above their frontal edges or stay fixed with modelling materials pulled towards them. Usually, the uppermost rigid plate represents a terrane of stronger lithosphere, and sometimes rigid blocks are used as indenters to simulate indention tectonics (e.g., Bonini et al., 1999; Persson, 2001).

Our study area, the northeastern Tibetan Plateau, is characterized by convergence between the stronger Qaidam Basin and the relatively weak Qilian Shan belt (e.g., Braitenberg et al., 2003; Zhang Z. et al., 2011). The indentation of the Qaidam Basin is also a popular model for explaining the structural evolution of the Qaidam-Qilian Shan belt (Cheng et al., 2015). Therefore, the latter rigid plate setup is adopted in this study (Figure 5A). We use two L-shaped thin metal plates (2 mm thick) to construct the basal velocity boundary conditions and provide experimental convergence for their overlying crust analogue (Figure 5A). The shorter (40 cm) plate A is superposed above the longer (99 cm) plate B, with its frontal edge acting as the S-point. The overlap between the two plates approximates the juxtaposition of natural overriding and subducting plates. The upper surface represents the mid-crustal detachment plane beneath the Qaidam Basin (Yin et al., 2008a) and the Qilian Shan belt (Gao et al., 1999; Ye et al., 2015). Notably, both end walls of the sandbox are mobile and can be used to drive motions of the basal plates. When moving the upper and shorter plate towards the right, the S-point also advances, acting as an analogue of the frontal edge of the indenting Qaidam Basin (Figure 5B). If only the lower plate is pushed from the left, the S-point remains fixed. This case is akin to pure underthrusting beneath the Qilian Shan belt (Figure 5C). More

complex convergence histories involving bidirectional compression (Gao et al., 1999; Zuza et al., 2019) and multiple stages of deformation (i.e., an inherited palaeo-Qilian Shan, Zhang et al., 2017; Cheng et al., 2018; Yu et al., 2019) are also easy to implement (see Table 1 for details).

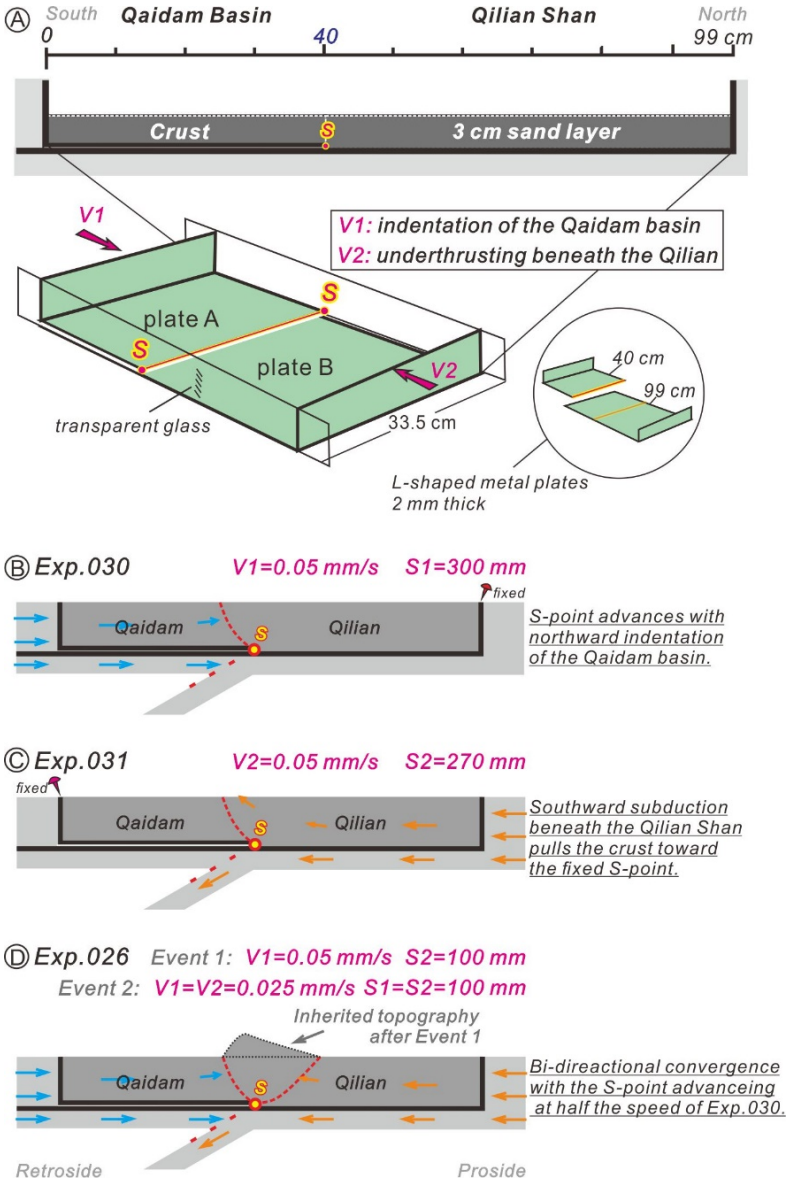

Figure 5 Schematic diagrams showing model set-up (A) and (B-D) three investigated end-member boundary conditions concerning different kinematics of mantle lithosphere. 2D and 3D cartoons in Figure A illustrating the deformation apparatus. Two L-shaped metal plates (in light green) are used. Their related motion deforms the overlying 3cm-thick sand layer. The shorter plate A is always situated above the longer plate B, with its velocity and shortening labeled as V1 and S1. While plate B's velocity and shortening are labeled as V2 and S2 in Table 1.

Table 1 Overview of presented experiments

Set 1: tests of different basal velocity boundary conditions		
Exp.030	V_1=0.05mm/s; S_1=300mm (northward indentation)	
Exp.031	V_2=0.05mm/s; S_2=270mm (southward subduction)	
Exp.026	V_1=0.05mm/s; S_1=100mm（*Event 1*）	V_1=V_2=0.025mm/s; S_1=S_2=100mm （*Event 2*）
Set 2: tests of inherited structures and topography		
Exp.022	V_2=0.05mm/s; S_2=100mm （*Event 1*）	V_1=0.05mm/s; S_1=200mm *(Event 2)*
Exp.020	V_1=0.05mm/s; S_1=100mm（*Event 1*）	V_2=0.05mm/s; S_2=200mm（*Event 2*）

Arbitrarily, we consider the boundary of Qaidam-Qilian beneath the southern Qilian Shan to be the S-point (Figure 2). This place is in the core of the doubly vergent Qaidam-Qilian wedge with the thickest crust and highest elevation in the region (Cui et al., 1995; Gao et al., 1999). Moreover, this belt has exposed a linear distribution of ultrahigh-pressure metamorphic rocks and is also a seismically active zone with concentrated earthquakes (Wei et al., 2010; Elliott et al., 2011; Han et al., 2019, Figure 1B), meaning that both long-term and short-term deformation have occurred around this boundary. However, note also that the results from our modelling would provide fundamental and spontaneous constraints on deep processes, which should be applicable to any places where they truly occur.

3.2 Modelling materials and scaling

Assemblages of sand obeying the same frictional failure law as brittle crustal rocks (e.g., Krantz, 1991; Lohrmann et al., 2003; Kilinkmüller et al., 2016; Reber et al., 2020) are excellent materials for use in sandbox modelling. The aeolian sand that we used was well rounded, with grain sizes of 0.2-0.3 mm and a density of ~1600 kg/m^3. With a Hubbert-type shear test box (e.g., Krantz, 1991), we measured the internal coefficient

of friction of the sand as ~0.4 and the cohesion as ~50 Pa, while the basal coefficient of friction (related to the metal plate) was ~0.3. To be representative of a natural setting, sandbox experiments should be properly scaled (Hubbert, 1937; Ramberg, 1981; Koyi, 1997). The scaling parameters can be expressed by the equation: $\frac{C_m}{C_n} = \frac{\rho_m \times l_m \times g}{\rho_n \times l_n \times g}$ (e.g., Schellart, 2000; Lohrmann et al., 2003; Corti et al., 2003), where ρ and l are the density and thickness of the brittle layer, respectively, c is the cohesion, and g is the gravitational acceleration (Table 2). The subscripts m and n indicate values for the model and nature, respectively. Taking the density and cohesion of natural crust rocks as 2800 kg/m^3 and 50 MPa (Jaeger et al., 2009), we calculate $l_m / l_n \approx 1.75\times10^{-6}$; thus, 1 cm in our sandbox corresponds to ~6 km in nature.

Table 2 Material properties and scaling ratios between model and nature

Quantity	Nature (n)	Model (m)	Scaling ratio (m/n)
Density (ρ)	2800 kg/m^3	1600 kg/m^3	~0.6
Layer Thickness (l)	18 km	3 cm	~1.75×10^{-6}
Gravity acceleration (g)	9.81 m/s^2	9.81 m/s^2	1
Cohesion (C)	50 MPa[a]	~50 Pa	1-3×10^{-6}
Internal friction coefficient (μ)	0.6-0.85[b]	~0.4	~1
Basal friction coefficient (μ_b)	/	~0.3	/

[a] Jaeger et al., 2009; [b] Byerlee, 1978;

3.3 Model construction and deformation

All presented sandbox experiments were performed in a glass-sided rectangular box with a horizontal basement. Its internal dimensions were 99 × 33.5 × 30 (length × width × height in cm). Within the sandbox, we built a 3 cm-thick, uniform sand pack (equivalent to 18 km in nature) as the mid-upper crust analogue of the northeastern

Tibetan Plateau (Figure 5A), assuming that the strength contrast between the Qaidam Basin and the Qilian Shan belt mainly relies on the lower crust and mantle lithosphere (Wei et al., 2010; Zhang et al., 2011; Gong et al., 2018), not on the crust investigated here. Two computer-driven motors were connected to the mobile backstops and provided experimental shortening. Frictional deformation is time independent; therefore, the experimental convergence rate does not affect the evolution of modelled thrust belts. We maintain the total convergence rate at 0.05 mm/s, regardless of unidirectional or bidirectional shortening (Figures 5B-D). The total amount of applied convergence was fixed at 300 mm (180 km in nature), except Exp.031 (Table 1).

To reduce local inhomogeneities, all sand was sieved into the sandbox from a fixed height of 40 cm relative to the basement. Before this, the lateral glass sidewalls were cleaned carefully and coated with friction-reducing talcum powder to minimize sidewall friction. To record the evolution of each experiment, lateral photographs were taken through the transparent sidewall at a shortening interval of 3 mm. The geometry and kinematics of the resultant thrust wedges were measured from these photographs. Particle image velocimetry (PIV) technology was also applied to calculate the incremental displacement and strain field of selected image sequences (e.g., Adam et al., 2005; Sun et al., 2019).

4 Modelling results

Five experiments are presented here (Table 1). The first three experiments in Set 1

illustrate the influence of distinct basal boundary conditions on the evolution of the overlying convergent belts, while the last two experiments in Set 2 demonstrate how inherited structure and topographic relief (produced by the first stage of convergence) affect successive deformation localization within evolving thrust wedges (during the second stage of convergence).

4.1 Set 1: Tests of different basal velocity boundary conditions

Three sandbox experiments employing distinct basal velocity boundary conditions are presented here, corresponding to hypothetical scenarios in which crustal convergence originates from northward indentation of the Qaidam Basin (e.g., Clark and Roydon, 2000; Tappinnor et al., 2001; Zhang et al., 2004; Cheng et al., 2015, Exp.030 in Figures 5B and 6A-F), slab pull exerted by southward underthrusting beneath the Qilian Shan belt (Ye et al., 2015; Zuza et al., 2016, Exp.031 Figures 5C and 6G-L), or bidirectional compression resulting from synchronous application of the two end member boundary conditions (Gao et al., 1999; Zuza et al., 2018, Exp.026 in Figures 5D and 6M-R). Next, we describe the structural and kinematical evolution of these experiments in detail (Figures 6 and 7) to illustrate how the deformation of the modelled crust changes with the underlying velocity boundary conditions.

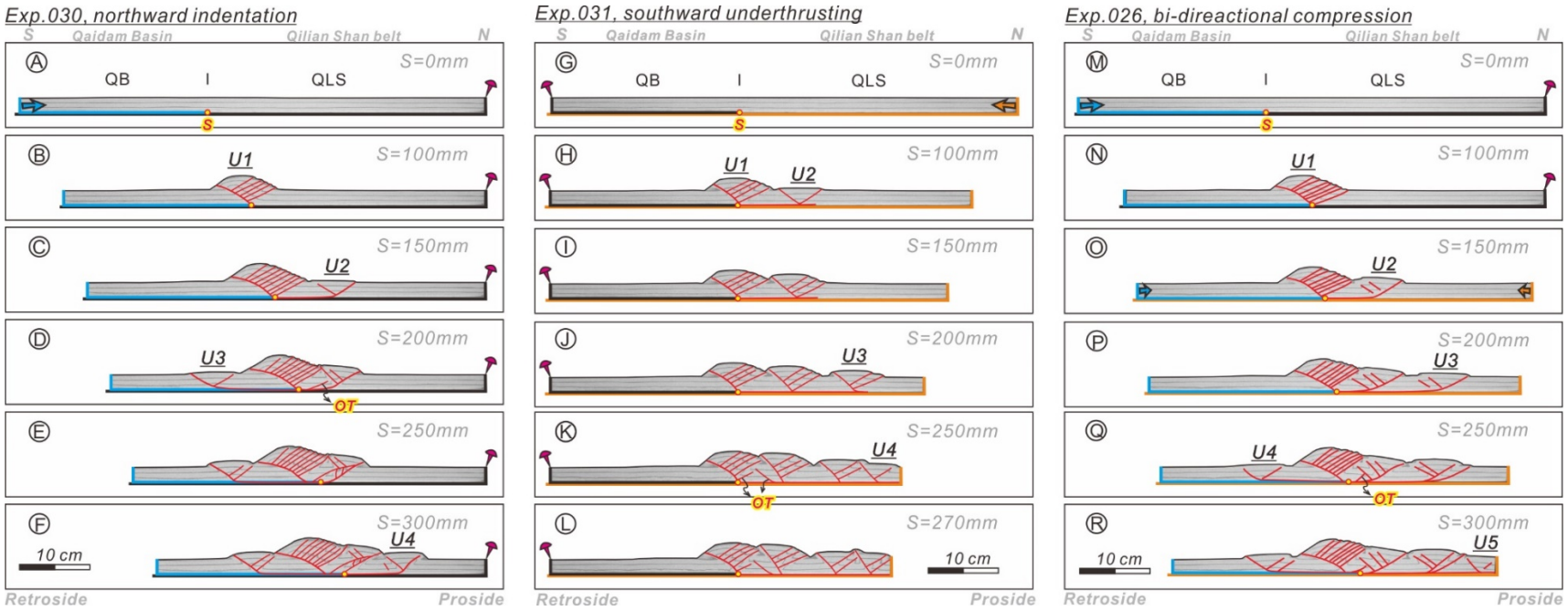

Figure 6 Evolutionary stages of three sandbox experiments testing different basal velocity boundary conditions. (A-F) Exp.030, northward indentation of the Qaidam Basin; (G-L) Exp.031, southward underthrusting beneath the Qilian Shan belt; (M-R) Exp.026, southward underthrusting joined in a later stage. Together with continuous northward indention, a bi-directional compression had formed. During this second event, convergence rate is the same with first event and the other experiments, but has been partitioned between two end member basal velocity boundary conditions; In these experiments, all basal plates that indicated by black color are fixed during the modeling. The blue and shorter basal plate indicates that it is droving the overlying sand pile to indent sand above the other plate, corresponding to northward of indentation of Qaidam Basin. While the orange basal plate is underthrusting beneath the fixed, shorter one through the S-point. In response, its overlying sand layer is transported toward and accretes against the sand above shorter plate, which is analogue to accretion of crustal materials induced by the southward subduction of NCC's mantle lithosphere. The basal velocity singularity, S-point is denoted by yellow dots. The pin indicates fixed end wall. U: uplift zone, labeled by Arabic number according to their sequence; OT: out of sequence thrust.

4.1.1 Exp.030, northward indentation of the Qaidam Basin

In Exp.030, the longer basal plate (in black colour) remained fixed. The shorter blue plate slipped on the fixed plate, driving the overlying Qaidam Basin (QB) northward into the Qilian Shan (QLS) on the other side (Figure 5B and 6A). Its frontal edge travelled northward, forming a mobile S-point at the base. Consistent with observations from previous studies (e.g., Del Castello et al., 2004; McClay and Whitehouse, 2004), initial deformation occurred immediately at this basal velocity discontinuity (S-point) (Figure 6B). The first deformation appeared as a pop-up structure (termed U1 hereafter). With convergence, the retro-vergent thrust beneath U1 (retro-thrust, tapering to the overlying slab) continued to take up a large amount of displacement, which contributed to continuous thickening of U1 and its increasing asymmetry. The pro-vergent thrust (pro-thrust, pointing to the downgoing slab) levelled up quickly and was replaced by in-sequence faults with similar properties. When the convergence amounted to 135 mm, a total of eight short-lived pro-thrusts had developed (Figure 6C), which along with the retro-thrust, elevated U1 to a height of ~65 mm at an average rate of 0.283 elevation/convergence (E/C) (Figure 7A). That was, one unit of convergence was converted to 0.283 units of vertical uplift during this initial stage.

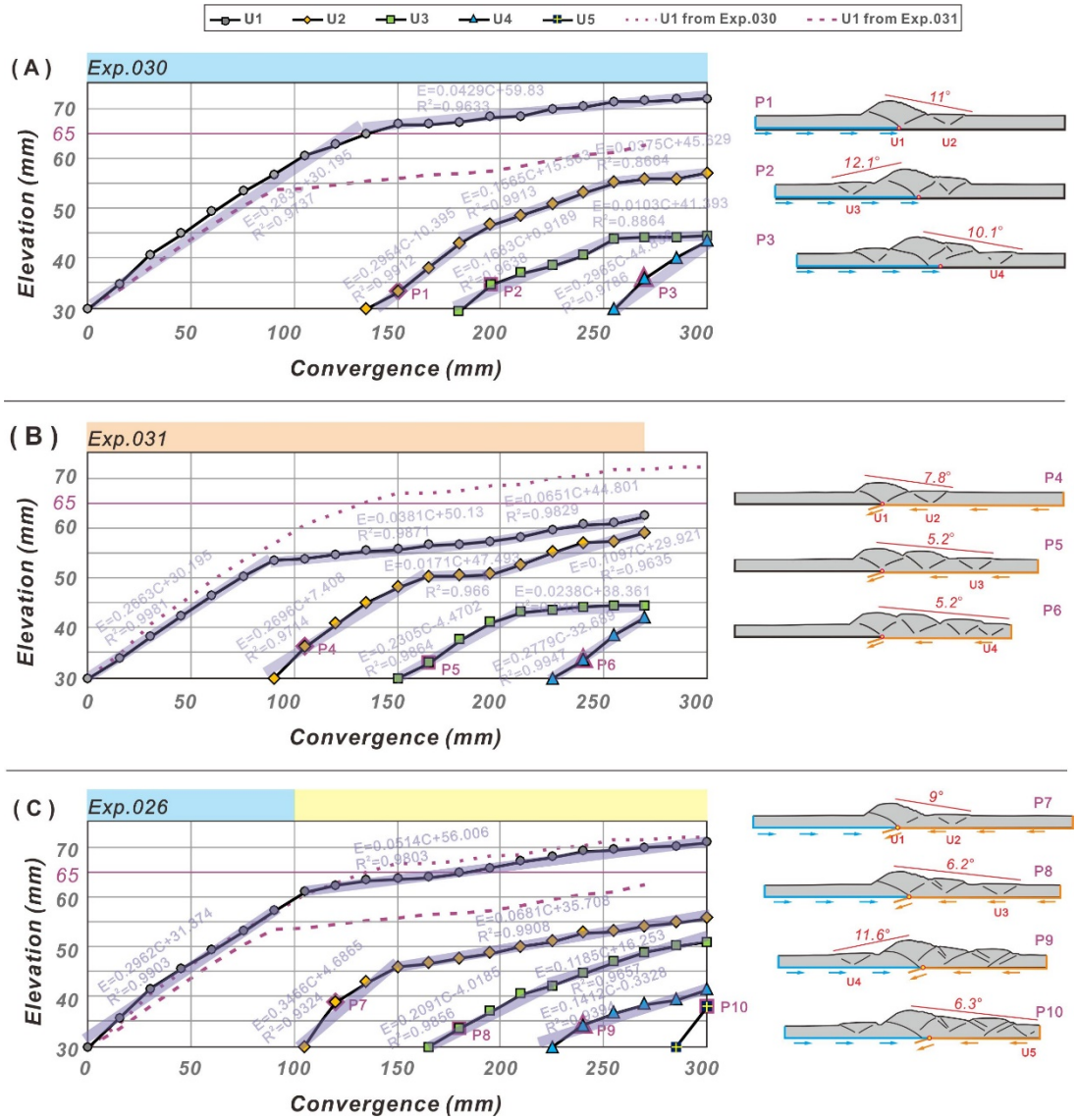

Figure 7 (A-C) Elevation versus convergence curves for each structure in each sandbox. Simplified line drawings of thrust wedges illustrating wedge geometry at onset of outward migration of the deformation front. To characterize uplift rates, liner fitted segments of each curves are also indicated by lilac thick lines. Segmentation are mainly determined by structural evolution of modeled thrust belts. Each effective segment must cover at least 45mm of convergence to ensure its representativeness. Simplified line drawings of thrust wedges illustrating wedge geometry at onset of the latest outward migration of deformation front. Noteworthy, U3 in Exp.030 developing in the other plate QB, does not correspond with U3 in Exp.031.

After this stage, lateral spreading of deformation from the S-point gave rise to the second pop-up structure U2 on the pro-side (Figure 6C). As the latest deformation front, U2 experienced rapid uplift with an E/C ratio of 0.285, while activation of U1 decreased

346 by 85% to 0.043 E/C (Figure 7A). At this time, the root of U1 was still coupled with
347 the moving S-point. When convergence reached 180 mm, the height of U1 increased to
348 ~68 mm, and deformation propagated outward again. The third pop-up structure U3
349 nucleated on the retro-side, showing a propagation direction opposite to that of U2
350 (Figure 6D). Notably, the formation of U3 here meant that the plane between the QB
351 analogue and the basal plate was activated as a detachment. U1 was decoupled from
352 the S-point, the whole thrust wedge slipped towards the retro-side, and an out-of-
353 sequence thrust (OT) developed ahead of the moving S-point (Figures 6D-E).
354 Interestingly, the initial uplift of U3 was relatively lower than those of U1 and U2 at
355 only 0.168 E/C. In response to its formation, the uplift rate of U2 on the other side
356 (related to the S-point in the middle) decreased to 0.157 E/C, ~53% of its initial value
357 (Figure 7A). Therefore, major convergence was localized evenly on the two edges of
358 the resultant doubly vergent thrust wedge. This situation was maintained at 255 mm of
359 convergence, and another pop-up structure U4 then took shape on the pro-side (Figure
360 6F). Its initial uplift rate was similar to those of U1 and U2, at ~0.296 E/C. During its
361 rapid uplift, all the other structures showed very low activity levels.

362 By the end, a total of 300 mm of experimental convergence was applied through
363 northward indentation of the QB crust analogue. It produced a relatively symmetric
364 doubly vergent thrust wedge (Figures 6D-F), with the maximum slope angles (achieved
365 when the new deformation front nucleated) for its retro-wedge and pro-wedge at 12.1°
366 and 11°-10.1°, respectively (Figure 7A).

4.1.2 Exp.031, southward underthrusting beneath the Qilian Shan

In this experiment, the longer basal plate underthrust southward at the S-point, beneath the fixed, shorter plate (Figure 5C). The overlying QLS crust analogue was transported towards and accreted against the fixed QB analogue above the shorter plate, which was analogous to the accretion of crustal materials induced by southward underthrusting beneath the QLS belt (Figures 6G-L).

Similar to Exp.030, the initial deformation still occurred in the region above the S-point and was also expressed by a pop-up structure U1 with one long-lived retro-thrust and several closely spaced short-lived pro-thrusts (Figures 6G-H). However, the period in which U1 in Exp.031 acted as the only active structure was much shorter, covering only the first 90 mm of convergence (Figure 7B). The number of pro-thrusts before lateral spreading of deformation was four, half of that in Exp.030. Moreover, as indicated by the E/C curve for U1, its initial uplift was 0.266 E/C, ~7% slower than its counterpart in Exp.030. Therefore, when the second pop-up structure U2 nucleated on pro-side of the S-point, the height of U1 was ~54 mm (Figure 7B), much smaller than U1 in Exp.030 at ~65 mm (Figure 7A).

After its formation, structure U2 replaced U1 in accommodating experimental convergence, with the initial uplift rate expressed as 0.270 E/C (Figure 7B). U1 lost most of its initial activation, uplifting slowly at a rate of 0.038 E/C. Similarly, when convergence continued to 150 mm, the third pop-up structure U3 developed in turn

ahead of U2 (Figure 6I-J). It obeyed the same law as U1 and U2 did; once the successor structure nucleated and behaved as the new deformation front, the activities of previous structures were greatly reduced by 90-95% (Figure 7B). Near the end, the last pop-up structure U4 nucleated, closely adjacent to the approaching end wall (Figures 6J-L). Undoubtedly, this structure was under the influence of the vertical end wall. However, its initial uplift progressed at a rate of 0.278 E/C, similar to other structures. Notably, the whole pro-side was fully occupied by thrust deformation after the formation of U4 and started being squeezed between the end wall in the north and the retro-thrust beneath U1. In response, two out-of-sequence faults nucleated beneath U1 and U2, which induced significant reactivation with their E/C ratios increasing from 0.038 and 0.017 to 0.065 and 0.110, respectively (Figure 7B). Specifically, in this stage, only U3 located between the reactivated U2 and the new deformation front U4 showed no reaction to the squeeze.

In response to 270 mm of southward underthrusting beneath the QLS analogue, a one-sided thrust wedge tapering only to the pro-side formed (Figures 6G-L). Its maximum slope angles were in the range of 7.8°-5.2°, showing much gentler surface topography with respect to counterparts in Exp.030.

4.1.3 Exp.026, synchronous application of two end member basal velocity boundary conditions (a bidirectional compression case)

Exp.026 is presented here, in which different boundary conditions were applied in two

stages. In the initial stage, northward indentation of the QB provided the first 100 mm of convergence, identical to Exp.030 (Figures 6M-N). In the second stage, two end member basal velocity boundary conditions were applied synchronously, forming bidirectional compression (Figures 6O-R). Each end provided 100 mm of convergence. The total convergence rate remained constant throughout the modelling. However, during the later stage, it was partitioned evenly and applied through the two end member boundary conditions.

The deformation in this experiment also started with a pop-up structure immediately above the S-point (Figure 6M-N), similar to the other experiments. During the initial stage, structure U1 experienced continuous uplift at a rate of 0.296 E/C (Figure 7C) and was the only active structure. When the convergence continued to 100 mm, U1 was elevated to ~60 mm. Notably, the presented structural configuration and kinematics were highly similar to those of Exp.030 during the corresponding evolutionary stage (Figures 6A-B).

The experimental evolution progressed to the second stage after 100 mm of convergence; in this stage, a bidirectional compression boundary condition provided further convergence (Figure 6O). The deforming system showed an immediate response to this change, with the second structure U2 nucleating to the north of U1. At its onset, U2 along with U1 formed a pro-side-tapering thrust wedge that gave a surface slope of 9° (Figure 7C). With further convergence, U2 was the major active structure, uplifting at a rate up to 0.347 E/C. U1 lost ~80% of its activity with the uplift rate decreasing to

0.051 E/C. Note that this initial uplift rate of U2 was larger than any other structures in Exp.030 and Exp.031 (Figures 7A-B), as well as its predecessor and successors in this experiment (Figure 7C). When convergence amounted to 165 mm, the deformation front still migrated to the pro-side, and the third pop-up structure U3 developed (Figure 6P). Interestingly, U2 and U3 at this point were isolated by a small but unambiguous gap. A similar phenomenon was also observed in Exp.031 (Figure 6J) but absent in Exp.030. At the onset of U3, the thrust wedge composed of U1, U2 and U3 displayed a gentle 6.2° slope. Then, the localization of major deformation switched from U2 to U3. The uplift rate of U2 decreased to 0.068 E/C, while the uplift of U3 occurred at 0.209 E/C.

When experimental convergence reached 225 mm, the deformation spread to the retro-side for the first time, generating U4 in the QB crust analogue (Figure 6Q). U1 and U4 at this point composed a retro-tapering thrust wedge sloping at 11.6°. The height of U1 reached ~68 mm at this time (Figure 7C). These geometries were close to those in Exp.030 when the same retro-side deformation spreading occurred (retro-wedge tapering at ~12.1° and U1 ~67 mm high, Figure 7A). In the following convergence, structure U4 showed a clearly lower uplift rate than the initial uplift rates of other structures at only 0.141 E/C. U3 on the other side of the S-point lost ~45% of its initial activity but still maintained a comparable uplift rate of 0.119 E/C. Thus, the two structures on the edges of the resultant thrust wedges had similar weights in accommodating regional convergence during this latest stage. Notably, similar

kinematics were also observed in Exp.030 (U2 and U3 in Figure 7A).

When the convergence reached 285 mm, the fifth structure U5 emerged closely adjacent to the north end wall of the sandbox (Figure 6R). At this moment, the resultant pro-side-tapering thrust wedge displayed a gentle taper angle of ~6.3° (Figure 7C). However, due to the limited convergence this structure experienced, its uplift rate was difficult to determine in this experiment. By considering Exp.030 and Exp.031 as two end member deformation styles associated with their special boundary conditions, the final thrust wedge presented in Exp.026 actually combined the well-developed retro-wedge from Exp.030 and the pronounced pro-wedge from Exp.031.

4.2 Set 2: tests of inherited structures and topography

In this set of experiments, two end member basal velocity boundary conditions were applied alternately (Figure 8). The thrust systems building in the first stage (100 mm of convergence) would be further deformed by the other type of basal boundary condition in the following stage (another 200 mm of convergence). In this manner, we studied how the superposed Cenozoic deformation in the NE Tibetan Plateau took place and evolved on the basis of pre-Cenozoic structures and topography. Two experiments, Exp.022 and Exp.020, corresponding to a lower (Wang et al., 2017, Exp.022) or higher (Zhang et al., 2017; Cheng et al., 2019; Yu et al., 2019, Exp.020) paleo-Qilian Shan are shown here.

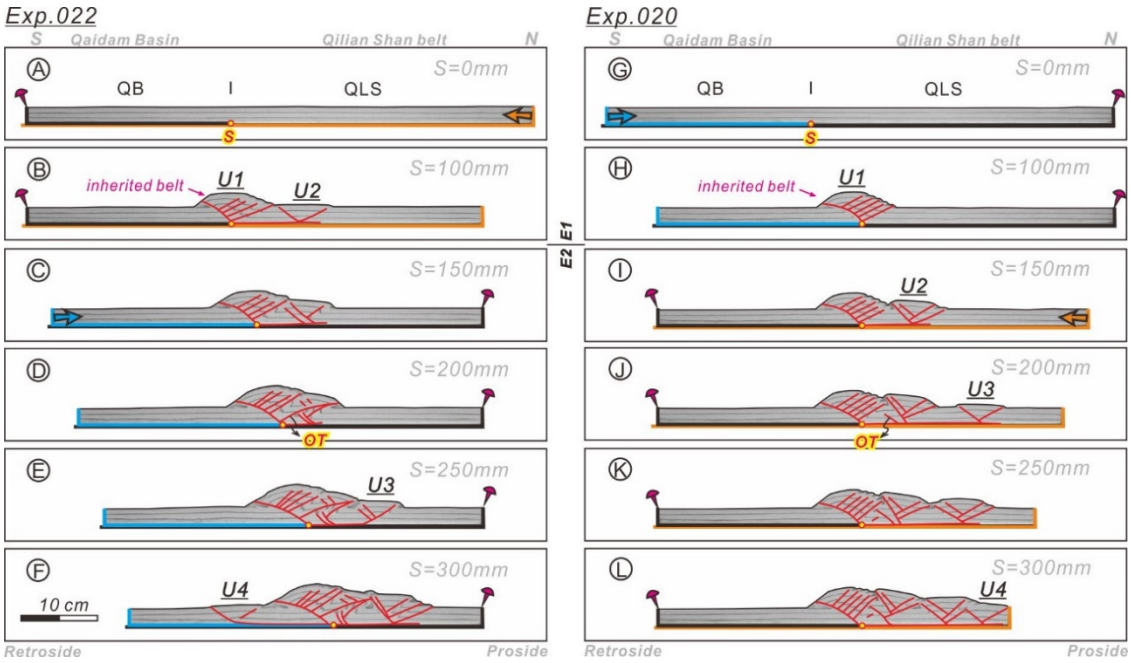

Figure 8 Evolutionary stages of two experiments testing the role of inherited structures and topography (i.e. paleo Qilian belt). (A-F) Exp.022 was an analogue case in which first stage of southward underthrusting beneath the QLS produced a wide but low relief inherited belt composed of two pop-up structures. Then this inherited belt was deformed by subsequent northward indentation of QB; (G-L) Exp.020 experienced a reverse sequence in related to Exp.022, with the first stage of convergence applied through northward indentation of the QB crust analog. The resultant inherited belt consisted of one highly elevated pop-up structure. E1/E2, the first/second event.

4.2.1 Exp.022, southward subduction beneath the QLS followed by northward indentation of the QB (a case of a wide but low-relief inherited belt)

In Exp.022, the first stage of deformation was driven by southward subduction beneath the QLS (Figures 8A-B). The resulting structural evolution was a perfect repetition of that of Exp.031, with the same in-sequence formation of U1 and U2 on the pro-side of the S-point (Figures 7A-B), similar uplift rates recorded for U1 (0.265 E/C) and approximately equal surface slopes (dipping at 7.9° towards the north) (Figure 9A).

Identical to Exp.031, deformation switched from U1 and spread laterally towards the pro-side at ~90 mm of convergence (Figure 8B). At the end of the first 100 mm of convergence, the height of U1 was ~55 mm. If the southward subduction had continued as in Exp.031, we could expect incremental deformation focusing on the front structure U2, while U1 entered a state of low activity (0.038 E/C in Figure 7B). However, the height of U1 at this time was significantly lower than the critical height that could motivate lateral deformation spread under pure northward indentation of the QB (~67 mm in Exp.030 as indicated by Figure 7A). Therefore, as a response to the new basal velocity boundary condition, U1 was reactivated. Its uplift rate increased from 0.038 E/C to 0.160 E/C within ~20 mm of convergence after the beginning of the second stage and lasted until the height of U1 was close to its counterpart in Exp.030 when experimental convergence amounted to ~200 mm (Figure 9A). During this period, a large-scale out-of-sequence pro-thrust occurred beneath U1 (Figures 8C-D). This fault, together with the retro-thrust originating from the S-point, constituted a conjugate pair of faults incorporating both U1 and U2, which acted as major structures to accommodate continuous indentation from the south. After ~200 mm of convergence, the E/C curve of U1 began to coincide with that from Exp.030 (Figure 9A), indicating that the major structural adjustment to alternation of the basal boundary condition had been completed. Notably, during this adjustment stage, the initial uplift of U2 was slower at only 0.214 E/C. This rate reflected the deformation partition between the reactivated U1 and the deformation front at this time.

When experimental convergence reached 225 mm, deformation migrated laterally again. Structure U3 nucleated and acted as the newest deformation front (Figure 8E), with an uplift rate reaching 0.293 E/C (Figure 9A). U3, along with U1 and U2, composed well-defined, north-tapering thrust wedges with an initial surface slope of 11°. With the convergence amounting to 255 mm, retro-ward deformation spread occurred, and U4 formed on the retro-side of the S-point. At its onset, U4 and U1 constituted a south-tapering thrust wedge (Figure 8F), displaying a surface slope of 12° (Figure 9A). The initial uplift of U4 at this time was slow, only half the rate of the other three structures at 0.133 E/C.

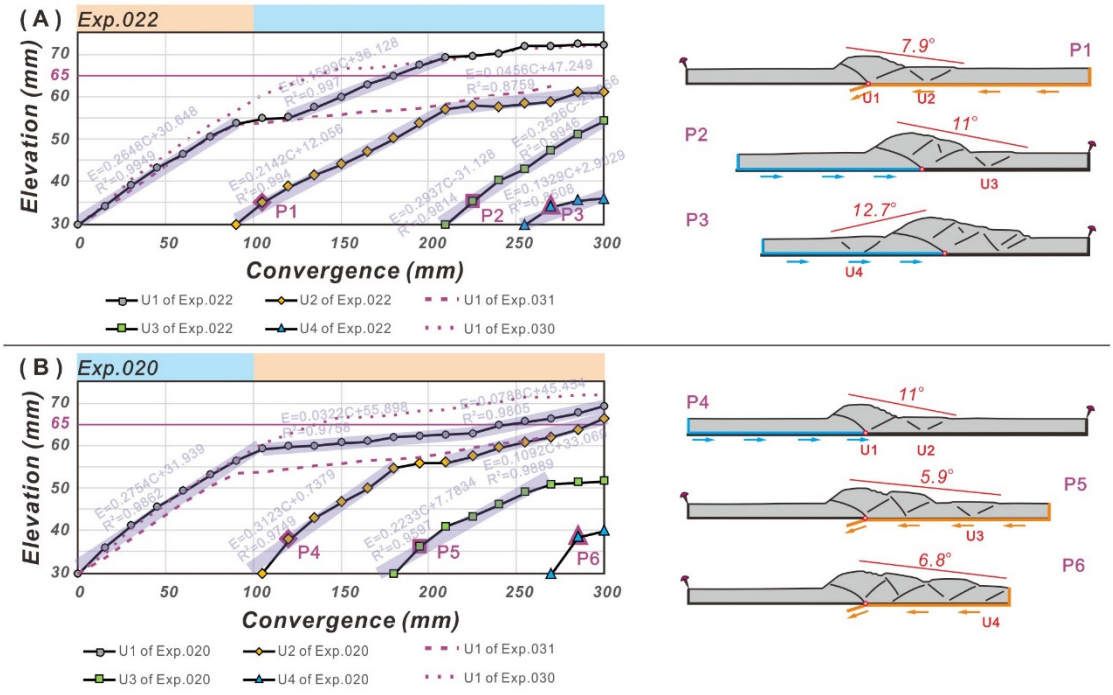

Figure 9 (A, B)-Elevation versus convergence curves for each structure in experiments of Set2. Simplified line drawings of thrust wedges illustrating wedge geometry at onset of outward migration of deformation front. Each effective segment must cover at least 45mm of convergence to ensure its representativeness.

4.2.2 Exp.020, southward subduction beneath the QLS replacing northward indentation of the QB in the later stage (a case of a narrow but high-relief inherited belt)

In Exp.020, the first 100 mm of convergence was applied through northward indentation of the QB (Figure 8G). Not surprisingly, the resultant structure and its evolution were similar to its counterparts in Exp.030 and Exp.031 (Figures 6B and 6N), as they had the same basal boundary condition. When the experimental convergence amounted to 100 mm, an inherited belt composed of one elevated pop-up structure U1 had formed (Figure 8H). Its height at this time reached ~60 mm (Figure 9B).

After this stage, the basal velocity boundary condition changed from northward indentation of the QB to later southward subduction beneath the QLS (Figure 8I). Such alternation immediately triggered lateral deformation propagation (Figure 9B). Notably, the height of U1 at this time was already greater than the critical height for deformation to migrate outward under pure southward underthrusting, which was ~54 mm, as observed in Exp.031 (Figure 6B). Therefore, when the second structure U2 nucleated, a relatively higher 11° surface slope angle appeared. After the formation of U2 on the pro-side, U1 lost most of its activity, with the uplift rate decreasing to 0.032 E/C. Instead, the main part of convergence was accommodated by U2 with an uplift rate up to 0.312 E/C.

When the convergence reached 180 mm, another outward deformation propagation

539 occurred with the formation of U3 ahead of U2 (Figure 8J). At this moment, U1, U2
540 and U3 formed a well-defined, pro-side-tapering thrust wedge. Its surface slope angle
541 at this time was 5.9°, slightly larger than its counterpart (5.2°) in Exp.031, due to a
542 higher U1 inherited from the first stage (Figure 9B). After approximately 30 mm of
543 convergence following the formation of U3, U1 and U2 started to be reactivated almost
544 simultaneously, with their uplift rates increasing from ~0.03 E/C to 0.079 E/C and 0.109
545 E/C, respectively. Synchronously, out-of-sequence faulting occurred beneath U1 and
546 U2. This faulting could be viewed as responses to the constrained foreland area, similar
547 to that in Exp.031 (Figure 7B). At 270 mm of convergence, the fourth structure U4
548 nucleated in the narrow area between the elevated U3 and the end wall (an analogue to
549 the boundary between the QLS and the NCC) (Figure 8K-L). The surface slope of the
550 resultant thrust wedge at this time was 6.8° (Figure 9B). After this point, the whole QLS
551 crust analogue was occupied by the one-sided thrust wedge and was squeezed
552 continuously, but no retro-side structure nucleated by the end with 300 mm of
553 convergence.

554 **4.3 A comparison of experimental observations**

555 All five experiments presented here can be viewed as five basal velocity boundary
556 conditions associated with different spatial combinations of two end member deep
557 geodynamic modes (northward indentation of the Qaidam Basin and southward
558 underthrusting beneath the Qilian Shan). Their structural evolutions differ to various
559 degrees and have interestingly intrinsic connections.

First, two experiments in which convergence is purely or predominantly applied by basal velocity boundary conditions corresponding with southward underthrusting (Exp.031 Figure 6G-L and Exp.020 Figure 8G-L) produce one-sided thrust wedges tapering mainly towards the pro-side. Their deformation initiates from the S-points at their base and then spreads towards the pro-side by in-sequence formation of pop-up structures. In their later stages, well-developed pro-wedges appear and display rather gentle slopes, tapering at 4°-7° (marked as Z1 in Figure 10). However, no deformation propagates to the retro-side during the applied experimental convergence. Instead, slumping of the axial zone occurs and produces retro-slump wedges sloping at 35°-40° (Z2 in Figure 10). Consequently, the resultant wedges are highly asymmetric (the large gap between Z1 and Z2 in Figure 10).

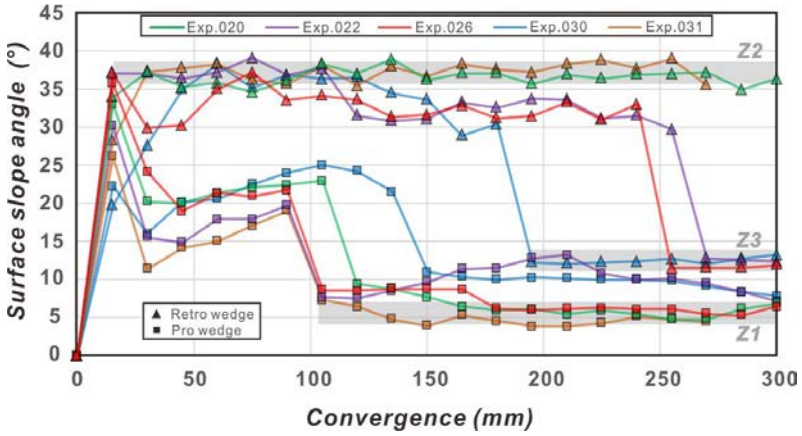

Figure 10 Surface slope angles of the pro- and retro- wedges in each experiment. Z1-Z3 are used to highlight special peaks presented during the experimental evolution. Their meanings are discussed in the text.

The two modelled thrust wedges have rather similar structural configurations, but significant kinematic differences emerge as responses to the variations in convergence

modes. The latest 200 mm of convergence in Exp.020 is applied through southward underthrusting, identical to Exp.031. However, before this stage, an elevated axial zone is inherited from a previous event. This higher inherited topography relief (related to that of Exp.031) changes deformation localization within the forming thrust wedge. For example, the heights of its following pop-up structures U2 and U3 are 55 mm and 50 mm by the end of their initial rapid uplift, respectively (Figure 9B). Both of them are ~5 mm higher than their counterparts in Exp.031 (50 mm and 45 mm, respectively, Figure 7B). Interestingly, the critical height of the axial zone achieved at the onset of U2 in Exp.020 is also ~5 mm higher than that in Exp.031. This phenomenon is consistent with the self-similar growth of fold-and-thrust belts as predicted by the critical taper theory (Davis et al., 1983; Dahlen, 1990). This quasi-uniform ~5 mm thickening recorded by U2 and U3 allows Exp.020 to eliminate the greater inherited topographic relief and achieve the same critical taper as in Exp.031 (Figure 10). However, as a side effect, during the later stage, the width of the deforming belt in Exp.020 is always narrower than that in Exp.031 (Figure 11).

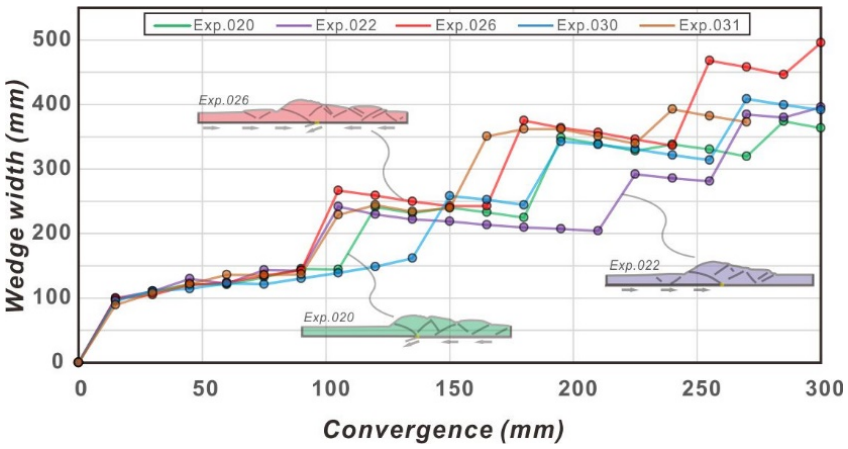

Figure 11 The width of thrust wedge formed in each experiment.

In contrast to one-sided wedges associated with southward underthrusting, northward indentation-dominated experiments, including Exp.030 (Figure 6A-F), Exp.026 (Figure 6M-R) and Exp.022 (Figure 8A-F), result in typical doubly vergent thrust wedges characterized by the presence of well-developed thrust-controlled retro-wedges. Deformation in these three experiments also initiates from the S-points and then propagates to the pro-side. However, this deformation mode is distributed by retro-side thrust accretion when a certain threshold is achieved (see next section for details). Additionally, the pro-wedges in Exp.030 and Exp.022 are much less developed than those in Exp.031 and Exp.020. This feature leads to a relatively symmetric wedge geometry in the two experiments. By comparison, the bidirectional compression Exp.026 develops a pro-wedge similar to those seen in Exp.031 and Exp.020 (Z1 in Figure 10) and a retro-wedge comparable with those in Exp.030 and Exp.022 (Z3 in Figure 10). Thus, the thrust wedge displays an intermediate geometry bridging the gap between one-sided and doubly vergent thrust wedges.

All the retro-wedges formed here display similar moderate slope angles (11°-13°, as indicated Z3 in Figure 10). However, their coupled pro-wedges on the other side vary. As shown in Figure 10, the surface slope angles of the pro-wedge in Exp.030 stabilize to a quasi-steady state value of 11° to 10° during the intermediate stage. After the latest pro-side deformation spreading at 255 mm of convergence (Figures 6E-F), the slopes decrease further to ~7° by the end. In Exp.022, the evolution of its pro-wedge surface slope is more complex. During the first outward deformation propagation, it first

615 increases from ~8° to 13° and then decreases to ~7° by the end. This process occurs
616 because in Exp.022, a deforming belt composed of two pop-up structures is inherited
617 from an earlier event (Figure 8B). Its height is much lower than the critical elevation
618 required for promoting the outward deformation to spread under the indentation type of
619 boundary condition. This situation results in out-of-sequence thrusting as structural
620 adjustment beneath the inherited belt (Figure 8C-E) and complicates the curve of slope
621 angles with local convexity. Notably, in both Exp.030 and Exp.022, indentation alone
622 drives the experimental convergence in this later stage. Therefore, they share similar
623 structural configurations and wedge geometries near their ends (see the lower blue and
624 purple branches between Z1 and Z3 in Figure 10).

625 Exp.026 inherits almost the same structure and topographic relief as that in Exp.030
626 after the first 100 mm of northward indentation. In the later event, the surface slope
627 angles of its resultant pro-wedge first stabilizes to 8°-9° and then quickly decreases to
628 a steady range of 4°-7°. Its slope angle curve deviates significantly from that of Exp.030;
629 instead, it more closely approximates those of underthrusting-dominated experiments
630 Exp.020 and Exp.031 (Z3 in Figure 10). In these later stages, underthrusting and
631 indenting take part in the experimental convergence of Exp.026 synchronously and
632 equally (Figure 6O). Therefore, it is not difficult to infer that underthrusting here
633 dominates this later-stage growth of the pro-wedge over the effects from ongoing
634 indentation. Moreover, such an effect originating from the participation of
635 underthrusting seems unrelated to the amount and applied velocity of underthrusting.

636 Because both of these factors in Exp .026 are much smaller than in the pure
637 underthrusting experiment Exp.031, their wedge width curves are rather similar (Figure
638 11).

639 Another feature to note is that the experimental convergence in both Exp.026 and
640 Exp.022 involves 100 mm of underthrusting and 200 mm of indentation, but their two
641 resultant thrust wedges show sharp contrasts (Figure 11), greatly highlighting the
642 sensitivity of thrust wedge evolution to the convergence histories investigated in this
643 study.

644 # 5 Discussion

645 ## 5.1 Effects of the applied basal velocity boundary conditions on lateral
646 deformation spreading

647 Generally, a convergent belt should have three major evolutionary stages, including
648 stage 1) formation of the axial zone above the S-point, 2) initiation of pro-side
649 deformation and 3) subsequent retro-side deformation propagation (Willett et al., 1993;
650 Naylor et al., 2005; Hoth et al., 2007). Certain thresholds are required for moving the
651 deforming system into the next stages (McClay and Whitehouse, 2004). In our sandbox
652 experiments, two types of thrust wedges appear, differing in whether a thrust-controlled
653 retro-wedge emerges. They actually represent convergent belts in two successive
654 evolutionary stages. However, our experimental series additionally emphasize that

655 histories of convergence (composition of indentation versus underthrusting) have
656 profound effects on the transitions between these successive evolutionary stages, which
657 has not been mentioned before.

658 The first structure nucleating immediately from the basal velocity discontinuity (S-
659 point) where one plate subducts beneath the other is usually called the axial zone
660 (Willett et al. 1993). Previous sandbox and numerical modelling studies revealed that
661 only when this axial zone achieves its critical height can lateral deformation initiate,
662 and the first step is always towards the pro-side (e.g., Wang and Davis, 1996; Storti and
663 Salvini, 2000; McClay and Whitehouse, 2004; Castello et al., 2005; Naylor and Sinclair,
664 2007; Hardy et al, 2009; Bigi et al., 2010). Formation and evolution of the axial zone
665 are the results of asymmetric basal velocity boundary conditions aside from the S-point.
666 The duration of its activation before the outward deformation stepping should be
667 controlled mainly by the strength of the simulation materials because during this stage,
668 the evolving topographic relief is too small to need support from the base (Naylor et al.,
669 2005).

670 In our sandbox, the only differences among the experiments presented here are the
671 applied basal velocity boundary conditions. The mode of initial deformation is similar
672 in all our experiments and consistent with observations from previous modelling studies.
673 However, the activation of axial zones varies, and their critical elevations are found to
674 depend strongly on the applied basal boundary conditions. For example, the underthrust
675 type of boundary condition with a fixed S-point, as in Exp.031, displays a lower critical

676 elevation, ~54 mm, which is achieved before ~100 mm of convergence (Figure 7B).
677 The indentation type of boundary condition in Exp.030 generates a much higher critical
678 elevation, up to 65 mm after ~135 mm of convergence (Figure 7A). The initial uplift
679 rate of the axial zone is also higher in the case of the indentation type of boundary
680 condition than in the underthrust case. As indicated in Figures 7A and 7B, their contrast
681 is not very great, 0.283 E/C versus 0.266 E/C. However, this contrast should be reliable
682 because such rates are consistent with those in the other three experiments during the
683 corresponding stage (violet dashed lines in Figures 7C, 9A and 9B). Accordingly, we
684 suggest that, when compared with a fixed S-point in underthrusting cases, the
685 advancing S-points associated with the indenting plate should have a certain dynamic
686 effect on enhancing deformation localization, which results in faster and longer
687 duration of activation as recorded by the axial zone and delays the occurrence of pro-
688 side deformation spreading.

689 After the first outward step of deformation, two of our experiments experiencing
690 convergence dominated by underthrusting (Exp.031 and Exp.020) continue their pro-
691 ward deformation spreading to the end (Figures 6L and 8L). By comparison, in the other
692 three experiments whose convergence is mostly driven by indentation (Exp.030,
693 Exp.026 and Exp.022), retro-ward spreading of deformation initiates after 180 mm, 225
694 mm and 255 mm of convergence, respectively. Interestingly, when retro-side
695 deformation occurs, the temporal elevations of the axial zones in these three
696 experiments are in the range of 68-72 mm (Figures 7A, 7C and 9A). While the final

heights of the axial zones in Exp.020 and Exp.031 are lower, ~69 mm and 63 mm, respectively (Figures 7B and 9B). Thus, there must be a second critical elevation determining whether retro-side deformation occurs. Moreover, during this outward deformation spreading stage, convergence in Exp.026 is induced by indentation and underthrusting at the same time. In contrast, both Exp.022 and Exp.030 are deformed solely by indentation. We therefore infer that the second critical elevation associated with retro-side deformation maybe not sensitive to the applied velocity boundary conditions as the first critical elevation for pro-side deformation propagation is.

5.2 Effects of inherited structures and topography on tectonic uplift

Three of our experiments (Exp.026, Exp.022 and Exp.020) experienced two successive tectonic events. The structures and topography inherited from the first event allow an assessment of their roles in the following events. Hereafter, we start by introducing common observations of tectonic uplift within all five resultant thrust wedges (Figure s7 and 9). Five groups including 36 linear fitting uplift rates can be summarized (Table 3) and related to different evolutionary stages as well as their structural positions. On this basis, we address and quantitatively discuss details about the effects of inherited belts by taking two one-event experiments (Exp.030 and Exp.031) as references.

Table 3 Uplift rates recorded by in modelled convergent belts

	Uplift rate [convergence interval] structure name/experiment name	**Notes**
Initial rapid uplift stage following structure nucleation, on the proside	1) 0.283 E/C [0-135mm] U1/Exp.030	
	2) 0.295 E/C [135-180mm] U2/Exp.030	
	3) 0.299 E/C [255-300mm] U3/Exp.030	
	4) 0.266 E/C [0-90mm] U1/Exp.031	
	5) 0.270 E/C [90-165mm] U2/Exp.031	
	6) 0.230 E/C [150-210mm] U3/Exp.031	*smaller/spontaneous*
	7) 0.278 E/C [225-270mm] U4/Exp.031	
	8) 0.296 E/C [0-90mm] U1/Exp.026	
	9) 0.347 E/C [105-150mm] U2/Exp.026	*largest*
	10) 0.209 E/C [165-225mm] U3/Exp.026	*smallest*
	11) 0.264 E/C [0-90mm] U1/Exp.022	
	12) 0.214 E/C [90-210mm] U2/Exp.022	*smaller*
	13) 0.293 E/C [210-255mm] U3/Exp.022	
	14) 0.275 E/C [0-90mm] U1/Exp.020	
	15) 0.312 E/C [105-180mm] U2/Exp.020	*larger*
	16) 0.223 E/C [180-270mm] U3/Exp.020	*smaller*
Reactivation stage	1) 0.065 E/C [195-270mm] U1/Exp.031	*foreland buttress*
	2) 0.110 E/C [195-270mm] U2/Exp.031	*caused squeeze*
	3) 0.079 E/C [225-300mm] U1/Exp.020	*foreland buttress*
	4) 0.109 E/C [210-300mm] U2/Exp.020	*caused squeeze*
	5) 0.160 E/C [120-210mm] U1/Exp.022	*spontaneous*
Rapid uplift stage after structure nucleation, on the retroside	1) 0.168 E/C [180-255mm] U3/Exp.030	
	2) 0.141 E/C [225-300mm] U4/Exp.026	
	3) 0.133 E/C [225-300mm] U4/Exp.022	
Uplifting on proside deformation front, synchronous with retroside activation	1) 0.157 E/C [180-210mm] U2/Exp.030	
	2) 0.119 E/C [225-300mm] U3/Exp.026	
	3) 0.253 E/C [255-300mm] U2/Exp.022	
Slow uplifting after nucleation of successive structure	1) 0.043 E/C [135-300mm] U1/Exp.030	
	2) 0.038 E/C [255-300mm] U2/Exp.030	
	3) 0.010 E/C [255-300mm] U3/Exp.030	
	4) 0.038 E/C [90-195mm] U1/Exp.031	
	5) 0.024 E/C [210-270mm] U3/Exp.031	
	6) 0.051 E/C [105-300mm] U1/Exp.026	
	7) 0.068 E/C [150-300mm] U2/Exp.026	
	8) 0.046 E/C [210-300mm] U2/Exp.022	
	9) 0.032 E/C [105-225mm] U1/Exp.020	

Segmentations summarized here must cover ≥45mm of convergence, to ensure their effectiveness and representative, see Figures 7 and 9 for their details.

(1) Rapid uplift stage after structure initiation on the pro-side, 0.209-0.347 E/C

This group includes 16 effective data points covering a wide range. Some extreme cases should be specified, as their presence is closely related to inherited structures and topography.

First, the high values greater than 0.300 E/C only occur twice, for the U2 structures of Exp.026 (Figure 7C) and Exp.020 (Figure 9B). These two experiments have similar inherited belts resulting from 100 mm of indentation in the first event. The subsequent tectonic events of both experiments involve underthrusting. As discussed above, these similarities mean that the height of the inherited belt is greater than the critical elevation of the second event. Therefore, we consider the occurrence of high uplift rates to reflect structural adjustments to the overly high inherited topographic relief. Interestingly, the following U3 structures show the two lowermost values at 0.209 E/C and 0.223 E/C. As noted, U3 in the reference experiment Exp.031 also has a small initial uplift rate at 0.231 E/C (Figure 7B). Thus, the alternation style presented here may be controlled partially by the continued structural adjustment to greater inherited topographic relief and partially by the spontaneous evolution associated with underthrusting.

The last lower value of 0.214 E/C is recorded by structure U2 in Exp.022 (Figure 9A). This experiment inherits a gentle but wide deformed belt composed of an axial zone U1 and a newly formed pop-up U2 (Figure 8B). When the second indentation-dominated event starts, the maximum elevation of U1 is ~55 mm, 10 mm lower than the critical

737 elevation under indentation, as in the other reference experiment Exp.030 (Figure 7A).
738 To compensate for this missing height, approximately 20 mm of convergence after the
739 beginning of the second event, a significant reaction of U1 is observed (Figure 9A).
740 During this period, convergence is partitioned on both U1 and U2. This partitioning
741 results in the low uplift rate observed for U2.

742 Except for the above extreme values reflecting structural adjustment to different
743 inherited belts, the other ten data in this group fall in the range of 0.266 E/C to 0.299
744 E/C. They represent spontaneous activity of pro-side structures during their initial stage.

745 (2) Reactivated stage, 0.065-0.160 E/C

746 This group has five effective data points. The largest value of 0.160 E/C is recorded by
747 U1 in Exp.022 (Figure 9A). In this experiment, the inherited elevation of the axial zone
748 U1 is smaller than that corresponding to the boundary condition during the second event.
749 Thus, significant part of the deformation has retreated from deformation front U2 that
750 developed in the first event. The other four data points are observed in Exp.031 and
751 Exp.020 when the evolving thrust wedges meet the foreland buttresses (end walls)
752 (Figures 6L and 8L). As responses, structures U1 and U2 in these experiments are
753 reactivated and uplifted at 0.065 E/C and 0.110 E/C in Exp.031 (Figure 7B) and 0.079
754 E/C and 0.109 E/C in Exp.020 (Figure 9B), respectively. Noteworthy, no reactivated
755 structures regain their initial uplift rates.

(3) Rapid uplift stage after structure initiation on the retro-side, 0.133-0.168 E/C

(4) Moderate-rate uplift on the pro-side front (synchronized with retro-side deformation recorded in group 3), 0.119-0.253 E/C

Thrust accretion of materials on the retro-side occurs three times, and three highly similar data points on their initial uplift are collected in group 3, including 0.168 E/C in Exp.030 (Figure 7A), 0.141 E/C in Exp.026 (Figure 7C) and 0.133 E/C in Exp.022 (Figure 9A). Such rates are approximately half of those (the initial rates) on the pro-side. During the same period, two deformation fronts on the other side are also uplifted at similar rates, 0.157 E/C in Exp.030 and 0.119 E/C in Exp.026. The pro-side deformation front in Exp.022 has a much higher uplift rate of 0.252 E/C. Notably, in our experiments, Exp.022 shows the best reactions to inherited topographic relief. Deformation localization within its wedge is greatly distributed by inherited topographic relief. Its influence may be the result of an abnormally high rate here.

(5) Slow uplift stage after nucleation of successive structure, 0.010-0.068 E/C

A total of nine effective data points are obtained in this group. They reveal that structures in our sandbox are not locked totally. Instead, certain extremely low levels of activities are maintained. This activity may result from the low strength of the sands used and the low coefficients of basal fiction, which can form a very wide active region with distributed deformation (Hardy et al., 2009; Meng and Hodgetts, 2019).

In summary, the above data for tectonic thickening reveal that inherited belts have variable effects on the evolution of the second event, depending on the relationship between their inherited elevations and the critical elevations associated with ongoing basal velocity boundary conditions. However, note also that introduced differences in the uplifts of individual structures from them, as well as other boundary conditions such as the confined foreland area, are significantly weaker than those arising from changes in structural evolutionary stages which define groups of uplifting rates.

5.3 Experimental limitations

In this study, we focus only on how the proposed deep geodynamic processes (indentation and underthrusting) can affect the overlying crustal deformation; we do not aim to reproduce the details of the NE Tibetan Plateau. Therefore, several experimental limitations are involved to keep the experiments as simple as possible. First, the rigid basement used in our sandbox experiments excludes the occurrence of plate flexure and isostatic compensation. Because the experimental convergence is applied through slipping of two thin basal plates, the influences of downgoing lower crust and lithospheric mantle are also not considered. Additionally, syn-tectonic sedimentation within the Qaidam Basin and erosion in the Qilian Shan belt should play important roles but are not incorporated into the modelling. However, some of our experiments reproduce first-order structural configurations and deformation localization styles similar to those of the NE Tibetan Plateau, while others do not. These results mean that although the above limitations exist, by analysing the presented

796 experimental results, we can still obtain reasonable constraints for the formation of the
797 current NE Tibetan Plateau.

798 **5.4 Comparison with the QB-QLS belt in northeastern Tibet**

799 Deformation features and wedge geometries in the QB-QLS belt and the five
800 experiments allow us to establish plausible linkages between them. One solid
801 characteristic of the Cenozoic QB-QLS belt is the double-sided migration of its
802 deformation, from the boundary between the QB and QLS towards both the south and
803 north (Figure 4 and references therein). As illustrated in our experimental series, such
804 a deformation style is favoured by northward indentation of the QB (Exp.030 in Figures
805 6A-F, Exp.026 in Figures 6M-R and Exp.022 in Figures 8A-F). If the experimental
806 convergence is dominated by southward underthrusting as in Exp.031 (Figures 6G-L)
807 and Exp.020 (Figures 8G-L), no significant deformation could propagate into the retro-
808 side (i.e. the QB side) and only limited collapse occurs adjacent to the axial U1
809 structures (the SQL belt). On the other hand, the QLS belt has a gentle, nearly flat
810 surface (Figure 4). As our experiments reveal, gentle slopes of the pro-side wedges (4-
811 7°) would occur when underthrusting progresses beneath them (Figure 10). If ongoing
812 convergence is applied by pure indentation as in Exp.030 and Exp.022, much steeper
813 slope angles (~10°) are present. Moreover, their resultant thrust wedges are rather
814 symmetric (Figures 6F and 8F), significantly deviating from the asymmetric QB-QLS
815 belt with a highly developed QLS (pro)wedge. Therefore, only Exp.026, which
816 experienced bidirectional convergence, seems to best fit the wedge geometry of the

817 current QB-QLS belt (Figure 12), everything considered.

818 The consistency between the QB-QLS wedge and modelled wedge in Exp.026 is
819 supported by more detailed deformation sequences. On seismic profiles, Yin et al.
820 (2008a) identified growth strata associated with the North Qaidam thrust belt (NQB),
821 which suggest that deformation near the boundary of the NQB and the South Qilan
822 Shan (SQL) started during the deposition of the Lulehe Formation (the base of Cenozoic
823 strata within the QB). Its exact period remains debatable, varying from 65-50 Ma (Ke
824 et al., 2013; Ji et al., 2017) to ~30 Ma (Wang et al., 2017; Nie et al., 2020), but both are
825 clearly earlier than the initiation age (~18-11 Ma Pang et al., 2019) of the latest cooling
826 event recorded by surficial structures in the NQB. These surficial structures originate
827 from roof thrusts above the buried southwest-tapering thrust wedge (Figure 12 in Yin
828 et al., 2008a). Their activation actually represents southward wedging from the SQL
829 (axial zone). More importantly, on the other side of the SQL, the area covering the
830 northeastern part of the Centre Qilian Shan (CQL) to the North Qilian Shan (NQL)
831 documents almost the same cooling event beginning at 17-8 Ma (Qi et al., 2016; Zheng
832 et al., 2017). These ages mean that at ~15 Ma, deformation of the QB-QLS belt had
833 spread laterally, with the NQB and NQL being activated synchronously as southern and
834 northeastern deformation fronts at this time (Figure 3).

835 Such evolution is largely reproduced by our Exp.026 (Figures 6 and 12). First, the
836 formation of axial zone U1 in Exp.026, taking place immediately above the block
837 boundary and characterized by vertical uplift (Figures 6M-N), should resemble the

earlier deformation near the NQB and SQL. The major fault RT1 (Figure 12), analogous to the NQBT, accumulates a large amount of top-to-the-south slip and may account for the growth structures observed by Yin et al. (2008a). However, during this period, such impacts cannot reach the interior part of the QB. Only when U1 is elevated to the critical value would basal detachment on the retro-side be activated, and deformation originating from the plate boundary would now propagate into retro-side (the QB) and produce U4 (the NQB) there (Figures 6P-R). Notably, between the initial thickening concentrated at the plate boundary and the subsequent retro-side deformation, pro-side deformation propagation also occurs, as expressed by formation of U2 and U3 that correspond well with the CQL and NQL.

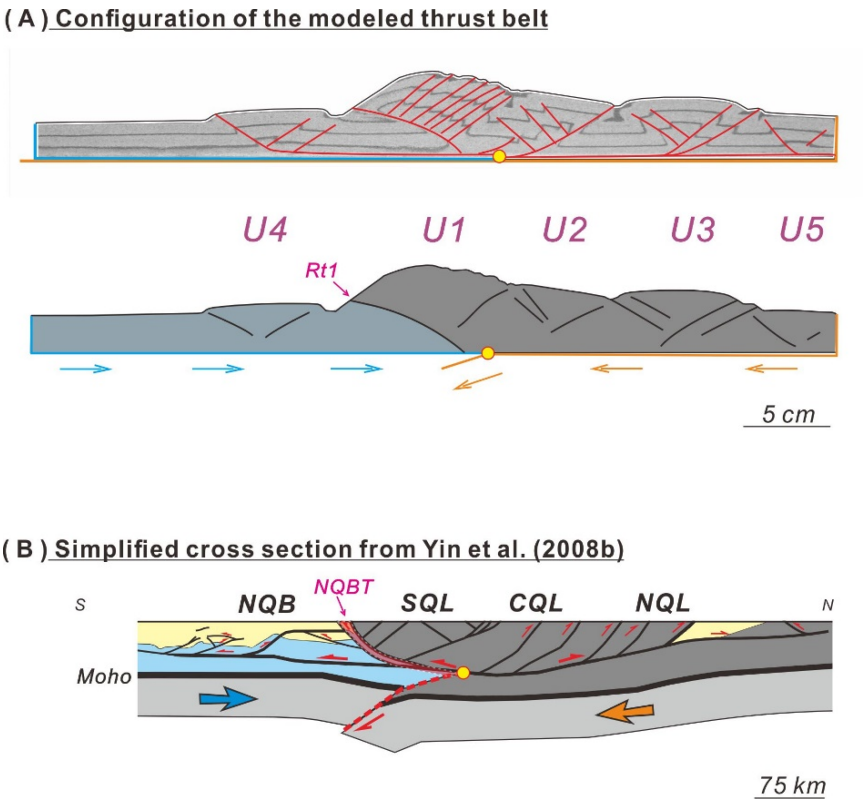

Figure 12 Comparison between (A) the modeled thrust wedge from Exp.026 after 300mm of convergence, and (B) simplified cross section from Yin et al. (2008b). U1-U5: uplift zones labeled

by their sequence. RT1: retro-thrust; NQB: Northeastern Qaidam basin, a southward tapering wedge beneath basin deposition had been imaged by seismic profiles (Yin et al., 2008a); NBQT: Northeastern Qaidam basin thrust system; SQL/CQL/NQL: Southern/Central/northeastern Qilian Shan belt. Notably, faults within the center of Qilian Shan part is more appropriate conceptualization on basis of the geophysical profile from Gao et al. (1999) in Figure 2.

Briefly, the doubly vergent thrust wedge produced by Exp.026, which experiences bidirectional convergence in the later evolutionary stage, approximates the QB-QLS belt in the first-order wedge geometry, topography and overall deformation sequence (Figure 12), implying later participation of southward underthrusting during the Cenozoic convergence of the QB-QLS belt (Gao et al., 1999; Zuza et al., 2018). Moreover, according to the experimental series, we could determine that southward underthrusting here promotes pro-side deformation spreading and contributes to the gentler surface slope of the QLS (Figures 11 and 13). While northward indentation enhances the deformation localization in front of the indenting QB, which facilitates achieving the critical elevation of the SQL for initiating deformation propagation into the QB.

5.5 Implications for seismicity within the western QB-QLS belt

The tectonically active NE Tibetan Plateau has recorded numerous earthquakes, including several catastrophic M>7 earthquakes, such as the 1927 M=8.3 Gulang event and the 1920 M=8.7 Haiyuan event. However, most of these earthquakes are concentrated on the edges of the QLS belt or closely associated with the Altyn Tagh and Haiyuan strike-slip faults (e.g., Tapponnier et al., 1990; Gaudemer et al., 1995;

873 Meyer et al., 1998; Chen et al., 1999), while the highly elevated SQL and CQL seem to
874 be avoided (Figures 1B and 2). Allen et al. (2017) also noted this blank area on their
875 seismicity map. Furthermore, they revealed that only a few M>5 thrust earthquakes
876 have occurred at elevations >3500 within the range and considered such phenomena as
877 a special state in the plateau formation.

878 Our modelling confirms this speculation and suggests that this correlation between high
879 seismicity and low topography around the QB-QLS belt should be evidence for ongoing
880 bidirectional convergence (Figure 13). Under a purely indenting-type boundary, a
881 sufficiently high axial zone is required to provide topographic loading that allows full
882 transport of northward motion (marked by dark blue) to the front of the modelled QLS
883 (e.g., ΔS=258-261 mm, Figure 13A). Otherwise, a certain amount of indentation would
884 be accommodated before reaching the northeastern front. At these moments, the edges
885 of the doubly vergent thrust wedge could concentrate deformation synchronously
886 (ΔS=192-195 mm and ΔS=255-258 mm). However, the present QLS deformation is
887 distributed within the relatively higher SQL and CQL, not outboard of them as is true
888 for its prototype (Figure 2). In the purely underthrusting-type boundary condition,
889 topographic loading of the axial zone protects the QB from the influence of
890 underthrusting beneath the QLS (Figure 13B). Deformation migrates within the
891 modelled QLS but not propagates into the QB part contrary to the intense seismicity
892 present near the NQB (Elliott et al., 2011; Han et al., 2019, Figure 2). Only when
893 indentation and underthrusting are applied synchronously can activation focused on

both edges of the modelled QB-QLS, as well as weak seismicity in the centre, be well reproduced under the aid of increased topographic loading, for example, at convergence increments ΔS=240-243 mm and ΔS=288-291 mm in Figure 13C.

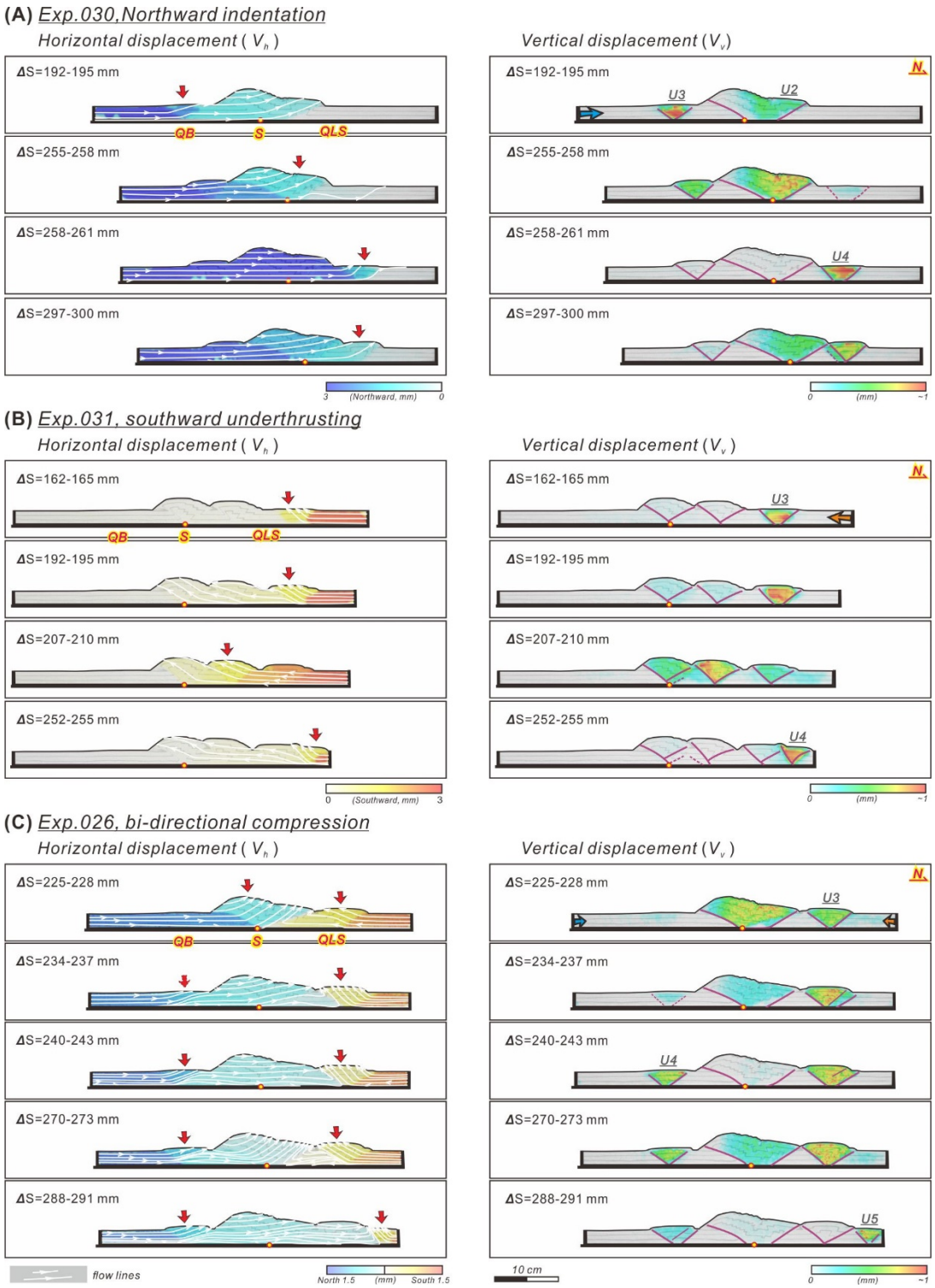

Figure 13 PIV analysis on kinematics of (A) Exp.030, (B) Exp.031 and (C) Exp.026, reflecting influences from distinct basal boundary conditions. Left to right show incremental horizontal and vertical displacement at the intervals of 3mm convergence. In the left, cold and warm colors are used to indicate displacement pointing to pro-/north and retro-/south side, respectively. The dark blue and brownish red areas are zones moving at the same speed as their underlying plates. A paler color represents a smaller speed, indicating the occurrence of detachment beneath. The reach of impacts exerted by each basal velocity boundary condition also have been indicated by their associated flow lines. Flow lines would be bended or disturbed when across the boundaries between different colors (active faults). At places where intensively uplifting occur, all or most of flow lines ramp up and break up to the surface. Only a small amount of flow lines at the deeper level may pass through and scatter over the next area, for example at ΔS=252-255mm in Figure 13B and ΔS=234-237mm in Figure 13C. Noteworthy, horizontal flow lines like ΔS=258-261mm in Figure 13A, represent rigid-block-like motion without internal deformation. Similar cases emerge in center of Exp.026 (Figure 13C) when incremental convergence reaches ΔS=240-243mm and ΔS=288-291mm, analogue to modern state of the QB-QLS belt shown in Figure 2.

5.6 Insights for the Cenozoic cooling event on the NE Tibetan Plateau

A rapid cooling event beginning at 10-15 Ma, with contemporaneous increased sediment accumulation in adjacent basins, has been identified in most areas of the northeastern Tibetan Plateau (e.g., Fang et al., 2007; Bush et al., 2016; Wang et al., 2017; He et al., 2018; Lu et al., 2018; Zhuang et al., 2018; Pang et al., 2019a). Previously, this widely distributed event has been considered a possible indicator for mantle removal or other shifts in regional geodynamics (boundary conditions and rheology as summarized in Yuan et al., 2013).

Our experimental series has explored two end member basal velocity boundary conditions (indentation of the QB and underthrusting beneath the QLS) and inherited structure and topographic relief (palaeo-relief of the QLS belt). Results confirm that these boundary conditions are capable of affecting uplift histories (uplift rates and

925 durations). However, their influences mainly focus on the axial zone U1structures (the
926 SQL) that nucleate above the plate boundary directionally and their successors U2 (the
927 CQL) (Figures 7 and 9), not on edges of the QB-QLS belt where the rapid exhumation
928 since 10-15 Ma has been observed (e.g., Yuan et al., 2013; Zhuang et al., 2018; Cheng
929 et al., 2019, Figure 3). Moreover, most of differences in uplift rate that result from
930 distinct boundary conditions are <0.05 E/C, close to 15-20% of variations, which may
931 be difficult to be reflected by thermochronological data from individual structures.
932 Therefore, varied boundary conditions investigated here alone is unlikely to induce the
933 widely distributed exhumation event; However, we note that this cooling event can be
934 considered as synchronous activation in two frontal parts of the QB-QLS belt (Figure
935 3), at least in its west segment (Figure 1). Notably, similar phenomenon has shown up
936 in each of our experiments that have evolved into retro-side deformation stage, and is
937 clearly recorded by their uplift curves (Figures 7A, 7C and 9A). Accordingly, we infer
938 that the rapid exhumation beginning at 10-15 Ma is an intrinsic feature reflecting
939 bidirectional deformation spreading from the elevated center of the doubly vergent,
940 QB-QLS thrust wedge.

941 Additionally, our experiments reveal that the changes in uplift of individual structures
942 depends more on the evolutionary stages of the modelled thrust wedges that contain
943 these structures. Up to one order of magnitude changes in uplift rates (0.346-0.010 E/C)
944 can be induced solely by the transition from one stage to the other (see section 5.2 for
945 details), values that are much greater than those arising from distinct boundary

conditions. Considering the modelled maximum rate of 0.300 E/C (that is, one unit of convergence can induce 0.3 unit of surface uplift on a certain structure) and regional convergence rates across the northeastern Tibetan Plateau of 4-10 mm/a (Zhang et al., 2004), the structural-controlled uplift (from the initiation of a certain structure to the occurrence of its successor) may reach 1.2-3 mm/a, which is not smaller than any reported rapid cooling rates (NQL: 0.5-1 mm/a, Zheng et al., 2010; 0.35-0.65 mm/a, Pang et al., 2019a; 1.7-2.3 mm/a, Hetzel et al., 2019; NQB-SQL: 0.62-2 mm/a, Pang et al., 2019b). In fact, episodic thrust activation resulting from evolutionary stage switching is an inherent attribute of evolving thrust wedges even under continuous and stable tectonics (e.g., Gutscher et al., 1996, 1998; Hoth et al., 2006; Naylor and Sinclair, 2007; Sun et al., 2016). Therefore, the role of evolutionary stage switching should not be neglected when interpreting thermochronological data from the northeastern Tibetan Plateau, which showing clear multi-stage deformation feature (e.g., Yuan et al., 2013; Zhuang et al., 2018; Li et al., 2020; Wang et al., 2020).

6 Conclusions

The formation of thrust wedges over two converging plates has been simulated by sandbox experiments. Two end member basal velocity boundary conditions analogous to northward indentation of the Qaidam Basin and southward underthrusting beneath the Qilian Shan belt have been taken into account and applied separately, alternately or synchronously in individual experiments to reproduce possible histories of boundary conditions in the northeastern Tibetan Plateau. The experimental results show that the

evolution of the modelled QB-QLS thrust belt is affected and perturbed to different degrees, depending on how the two end member boundary conditions participate in the experimental convergence, providing the following:

1) Certain critical elevations for the axial zone (originating from the plate boundary, corresponding with the southern Qilian Shan) determine lateral deformation propagation towards both sides of the plate boundary. The critical elevation for pro-side deformation propagation (towards the Qilian Shan belt) is greater under the indenting-type boundary condition than under the underthrusting-type boundary condition. While the critical elevation for retro-side deformation propagation (towards the Qaidam Basin) seems approximate regardless of the variable boundary conditions.

2) The relationship between inherited topographic relief (the palaeo-Qilian Shan) and critical elevation of certain boundary conditions controls the responses of inherited belt to successive tectonic event. Only when the former is smaller than the later one, immediate uplift would occur at the axial zone. Otherwise, subsequent deformation tends to focus on the edge of elevated inherited belt.

3) Shifts in boundary conditions such as inherited topographic relief or later joining of underthrusting would not introduce great changes in the uplift rates of individual structures. By comparison, variations induced by the switch in the structural evolutionary stage within thrust wedges can be up to one order of magnitude in

uplift rate.

One of our experiments investigating synchronous northward indentation and southward underthrusting produces the best-fit thrust wedge for the Qaidam-Qilian Shan thrust belt in terms of surface relief, wedge expansion mode and deformation localization, suggesting that the bi-compressional boundary condition proposed by Gao et al. (1999) and Zuza et al. (2016, 2018) may approximate the real, late Cenozoic situation more closely than the single directional conditions. Detailed insights for the Cenozoic growth of the northeastern Tibetan Plateau including:

4) With a fixed 180 km of overall convergence (300 mm in our sandbox), only when indentation of the Qaidam Basin reaches two-thirds or more can a mature doubly vergent thrust wedge alike to the Qaidam-Qilian Shan belt form. Otherwise, a retro-side thrust wedge (i.e. the northern Qaidam wedge, Yin et al. 2008a) cannot emerge.

5) Underthrusting beneath the Qilian Shan belt should have contributed to the gentle surface of the overlying Qilian Shan wedge, at least partially.

6) The present correlation between high seismicity and low elevation around the elevated southern-central Qilian Shan is controlled by bidirectional compression and regional topographic loading.

7) In the Qaidam-Qilian Shan belt, the widely distributed rapid exhumation beginning

at 10-15 Ma is an intrinsic feature associated with bidirectional deformation spreading of a doubly vergent thrust wedge.

Acknowledgements:

This work was jointly supported by the National Natural Science Foundation of China (41902201, 41590861, 41772209), the Second Tibetan Plateau Scientific Expedition and Research Program (STEP)(2019QZKK0901) and Guangdong Province Introduced Innovative R&D Team of Geological Processes and Natural Disasters around the South China Sea (2016ZT06N331); We are very grateful to Dr. Wang Yang and Liang Hao for their valuable discussions. All data sets for this research have been presented in the figures and tables.

References

Adam, J., Urai, J., Wieneke, B., Oncken, O., Pfeiffer, K., Kukowski, N., ... & Schmatz, J. (2005). Shear localisation and strain distribution during tectonic faulting—new insights from granular-flow experiments and high-resolution optical image correlation techniques. Journal of Structural Geology, 27(2), 283-301.

Allen, M. B., R. J. Walters, S. Song, C. Saville, N. De Paola, J. Ford, Z. Hu, and W. Sun (2017), Partitioning of oblique convergence coupled to the fault locking behavior of fold-and-thrust belts: Evidence from the Qilian Shan, northeastern Tibetan Plateau, Tectonics, 36, 1679–1698, doi:10.1002/2017TC004476.

Bao, X., Song, X., Xu, M., Wang, L., Sun, X., Mi, N., Yu, D., & Li, H. (2013). Crust and upper mantle structure of the North China Craton and the NE Tibetan Plateau and its tectonic implications. Earth and Planetary Science Letters, 129-137.

Beaumont, C., Ellis, S., & Pfiffner, A. (1999). Dynamics of sediment subduction-accretion at convergent margins: short-term modes, long-term deformation, and tectonic implications. Journal of Geophysical Research: Solid Earth, 104.

Bigi, S., Di Paolo, L., Vadacca, L., & Gambardella, G. (2010). Load and unload as interference factors on cyclical behavior and kinematics of Coulomb wedges: Insights from sandbox experiments. Journal of Structural Geology, 32(1), 28-44.

Bonini, M., Sokoutis, D., Talbot, C. J., Boccaletti, M., & Milnes, A. G. (1999). Indenter growth in analogue models of Alpine-type deformation. Tectonics, 18(1), 119-128.

Bush, M. A., Saylor, J. E., Horton, B. K., & Nie, J. (2016). Growth of the Qaidam Basin during Cenozoic exhumation in the northeastern Tibetan Plateau: Inferences from depositional patterns and multiproxy detrital provenance signatures. Lithosphere, 8(1), 58-82.

Burchfiel, B. C., Quidong, D., Molnar, P., Royden, L. H., Yipeng, W., Peizhen, Z., & Weiqi, Z. (1989). Intracrustal detachment within zones of continental deformation. Geology, 17(8), 748-752.

Braitenberg, C., Wang, Y., Fang, J., & Hsu, H. T. (2003). Spatial variations of flexure parameters over the Tibet-Quinghai plateau. Earth and Planetary Science Letters, 205(3), 211-224.

Byerlee, J., 1978. Friction of rocks. Pure Appl. Geophys. 116, 615 – 626. https://doi.org/10.1007/BF00876528.

Chen, W., Chen, C., & Nabelek, J. L. (1999). Present-day deformation of the Qaidam basin with implications for intra-continental tectonics. Tectonophysics, 305(1), 165-181.

Cheng, F., Jolivet, M., Dupont-Nivet, G., Wang, L., Yu, X., Guo, Z., 2015. Lateral extrusion along the Altyn Tagh Fault, Qilian Shan (NE Tibet): insight from a 3D crustal budget. Terra Nova 27 (6), 416–425.

Cheng, F., Garzione, C. N., Mitra, G., Jolivet, M., Guo, Z., Lu, H., Li, X., Zhang, B., Zhang, C., Zhang, H., & Wang, L. (2018). The interplay between climate and tectonics during the upward and outward growth of the Qilian Shan orogenic wedge, northeastern Tibetan Plateau. Earth-Science Reviews, 198, 102945.

Cheng, F., Garzione, C. N., Jolivet, M., Guo, Z., Zhang, D., Zhang, C., & Zhang, Q. (2019). Initial Deformation of the Northeastern Tibetan Plateau: Insights From Deposition of the Lulehe Formation in the Qaidam Basin. Tectonics, 38(2), 741-766.

Clark, M. K., & Royden, L. H. (2000). Topographic ooze: Building the eastern margin of Tibet by lower crustal flow. Geology, 28(8), 703-706.

Clark, M. K. (2012). Continental collision slowing due to viscous mantle lithosphere rather than topography. Nature, 483(7387), 74-77.

Corti, G., Bonini, M., Conticelli, S., Innocenti, F., Manetti, P., & Sokoutis, D. (2003). Analogue modelling of continental extension: a review focused on the relations between the patterns of deformation and the presence of magma. Earth-Science Reviews, 63(3), 169-247.

Cui Zuozhou, Li qiusheng, Wu chaodong, Yin zhouxun and Liu hongbing, 1995. The crustal and deep structures in Golmud- Ejin qi GGT. Chinese Journal of Geophysics, 38(s2): 15–28 (in Chinese).

Dahlen, F. A. (1990), Critical taper model of fold-and-thrust belts and accretionary wedges, Annu. Rev. Earth Planet. Sci., 18, 55–99.

Davis, D., J. Suppe, and F. A. Dahlen (1983), Mechanics of fold-and-thrust belts and accretionary wedges, J. Geophys. Res., 88, 1153–1172, doi:10.1029/JB088iB02p01153.

Del Castello, M., G. A. Pini, and K. R. McClay (2004), Effect of unbalanced topography and overloading on Coulomb wedge kinematics: Insights from sandbox modeling, J. Geophys. Res., 109, B05405, doi:10.1029/2003JB002709.

Del Castello, M., K. R. McClay, and G. A. Pini (2005), Role of preexisting topography and overburden on strain partitioning of oblique doubly vergent convergent wedges, Tectonics, 24(6), TC6004, doi:10.1029/2005TC001816.

Elliott, J. R., Parsons, B., Jackson, J., Shan, X., Sloan, R. A., & Walker, R. T. (2011). Depth segmentation of the seismogenic continental crust: The 2008 and 2009 Qaidam earthquakes. Geophysical Research Letters, 38(6).

Fang, X., Zhang, W., Meng, Q., Gao, J., Wang, X., King, J. W., ... & Miao, Y. (2007). High-resolution magnetostratigraphy of the Neogene Huaitoutala section in the eastern Qaidam Basin on the NE Tibetan Plateau, Qinghai Province, China and its implication on tectonic uplift of the NE Tibetan Plateau. Earth and Planetary Science Letters, 258(1), 293-306.

Feng, M., P. Kumar, J. Mechie, W. Zhao, R. Kind, H. Su, G. Xue, D. Shi, H. QianStructure of the crust and mantle down to 700 km depth beneath the East Qaidam basin and Qilian Shan from P and S receiver functions. Geophys. J. Int., 199 (2014), 3 (1). 1416-1429

Fielding, E. J., Isacks, B. L., Barazangi, M., & Duncan, C. C. (1994). How flat is Tibet. Geology, 22(2), 163-167.

Han, Cunrui, H., Zhouchuan, H., Mingjie, X., Liangshu, W., Ning, M., & Dayong, Y., & Hua., L. (2019). Focal mechanism and stress field in the northeastern Tibetan plateau: insight into layered crustal deformations. Geophysical Journal International. 218, 2066-2078.

Hardy, S., McClay, K., & Muñoz, J. A. (2009). Deformation and fault activity in space and time in high-resolution numerical models of doubly vergent thrust wedges. Marine and Petroleum Geology, 26(2), 232-248.

He, P., C. Song, Y. Wang, L. Chen, P. Chang, Q. Wang, and B. Ren (2017), Cenozoic exhumation in the Qilian Shan, northeastern Tibetan Plateau: Evidence from detrital fission track thermochronology in the Jiuquan Basin, J. Geophys. Res. Solid Earth, 122, 6910–6927, doi:10.1002/2017JB014216.

He, P., Song, C., Wang, Y., Meng, Q., Chen, L., Yao, L., ... & Chen, S. (2018). Cenozoic deformation history of the Qilian Shan (northeastern Tibetan Plateau) constrained by detrital apatite fission-track thermochronology in the northeastern Qaidam Basin. Tectonophysics, 1-11.

Hetzel, R., Hampel, A., Gebbeken, P., Xu, Q., & Gold, R. D. (2019). A constant slip rate for the western Qilian Shan frontal thrust during the last 200 ka consistent with GPS-derived and geological shortening rates. Earth & Planetary Science Letters, 509, 100-113.

Hoth, S., Hoffmann-Rothe, A., and Kukowski, N., 2007, Frontal accretion: An internal clock for bivergent wedge deformation and surface uplift: Journal of Geophysical Research, 112, B06408, doi: 10 .1029 /2006JB004357

Hu, X., Chen, D., Pan, B., Chen, J., Zhang, J., Chang, J., ... & Zhao, Q. (2019). Sedimentary evolution of the foreland basin in the NE Tibetan Plateau and the growth of the Qilian Shan since 7 Ma. Geological Society of America Bulletin, 1744-1760.

Hubbert, M. K. (1937). Theory of scale models as applied to the study of geologic structures. Geological Society of America Bulletin, 48(10), 1459-1520.

Gaudemer, Y., Tapponnier, P., Meyer, B., Peltzer, G., Shunmin, G., Zhitai, C., ... & Cifuentes, I. (1995). Partitioning of crustal slip between linked, active faults in the eastern Qilian Shan, and evidence for a major seismic gap, the 'Tianzhu gap', on the western Haiyuan Fault, Gansu (China). Geophysical Journal International, 120(3), 599-645.

Gan, W., P. Zhang, Z.-K. Shen, Z. Niu, M. Wang, Y. Wan, D. Zhou, and J. Cheng (2007), Present-day crustal motion within the Tibetan Plateau inferred from GPS measurements, J. Geophys. Res., 112, B08416, doi:10.1029/2005JB004120.

Gao, R., Cheng, X. Z., & Wu, G. J. (1999). Lithospheric structure and geodynamic model of the Golmud-Ejin transect in northeastern Tibet, in Macfarlane, A., Sorkhabi, R. B., and Quade, J., eds., Himalaya and Tibet: Mountain Roots to Mountain Tops: Boulder, Colorado, Geological Society of America Special Paper 328. 9-17.

Gong, W., Jiang, X., Zhou, H., Xing, J., Li, C., & Yang, K. (2018). Varied thermo-rheological structure, mechanical anisotropy and lithospheric deformation of the southeastern Tibetan plateau. Journal of Asian Earth Sciences, 163(SEP.1), 108-130.

Gutscher, M., Kukowski, N., Malavieille, J., & Lallemand, S. (1996). Cyclical behavior of thrust wedges: Insights from high basal friction sandbox experiments. Geology, 24(2), 135-138.

Gutscher, M., Kukowski, N., Malavieille, J., & Lallemand, S. (1998). Episodic imbricate thrusting and underthrusting: Analog experiments and mechanical analysis applied to the Alaskan Accretionary Wedge. Journal of Geophysical Research, 10161-10176.

Jaeger, J.C., Cook, N.G., Zimmerman, R., 2009. Fundamentals of Rock Mechanics. John Wiley & Sons.

Ji, J., Zhang, K., Clift, P.D., Zhuang, G., Song, B., Ke, X., Xu, Y., 2017. High-resolution

magnetostratigraphic study of the Paleogene-Neogene strata in the Northeastern Qaidam Basin: implications for the growth of the Northeastern Tibetan Plateau. Gondwana Res. 46, 141–155.

Jian, X., Guan, P., Zhang, W., Liang, H., Feng, F., & Fu, L. (2018). Late Cretaceous to early Eocene deformation in the northeastern Tibetan Plateau: Detrital apatite fission track evidence from northeastern Qaidam basin. Gondwana Research, 94-104.

Jolivet, M., Brunel, M., Seward, D., Xu, Z., Yang, J., Roger, F., ... & Wu, C. (2001). Mesozoic and Cenozoic tectonics of the northeastern edge of the Tibetan plateau: fission-track constraints. Tectonophysics, 343(1), 111-134.

Ke, X., Ji, J.J., Zhang, K.X., Kou, X.H., Song, B.W., Wang, C.W., 2013. Magnetostratigraphy and anisotropy of magnetic susceptibility of the lulehe formation in the Northeastern Qaidam basin. Acta Geol. Sin. 87:576–587. http://dx.doi.org/10.1111/1755-6724. 12069

Kind, R., Yuan, X., Saul, J., Nelson, D., Sobolev, S., Mechie, J., Zhao, W., Kosarev, G., Ni, J., Achauer, U., 2002. Seismic images of crust and upper mantle beneath Tibet: evidence for Eurasian plate subduction. Science. 298 (5596), 1219–1221.

Klinkmüller, M., Schreurs, G., Rosenau, M., & Kemnitz, H. (2016). Properties of granular analogue model materials: a community wide survey. Tectonophysics, S0040195116000548.

Koons, P.O., 1990, The two-sided orogen: Collision and erosion from the sand box to the Southern Alps, New Zealand: Geology, 18, 679–682, doi:10.1130/0091-7613(1990)018<0679:TSOCAE>2.3.CO;2.

Koyi, H. (1997). Analogue modelling from a qualitative to a quantitative technique - A Historical Outline. Journal of Petroleum Geology, 20(2), 223-238.

Krantz, R. W. (1991), Measurements of friction coefficients and cohesion for faulting and fault reactivation in laboratory models using sand and sand mixtures, Tectonophysics, 188(1), 203–207.

Li, H., Y. Shen, Z. Huang, X. Li, M. Gong, D. Shi, E. Sandvol, and A. Li (2014), The distribution of the mid-to-lower crustal low-velocity zone beneath the northeastern Tibetan Plateau revealed from ambient noise tomography, J. Geophys. Res. Solid Earth, 119, 1954–1970, doi:10.1002/2013JB010374

Li, B., Zuza, A. V., Chen, X., Hu, D., & Xiong, X. (2020). Cenozoic multi-phase deformation in the Qilian shan and out-of-sequence development of the northern tibetan plateau. Tectonophysics, 228423, doi.org/10.1016/j.tecto.2020.228423

Liang, X., Sandvol, E., Chen, Y. J., Hearn, T., Ni, J., Klemperer, S., ... & Tilmann, F. (2012). A complex Tibetan upper mantle: A fragmented Indian slab and no south-verging subduction of Eurasian lithosphere. Earth and Planetary Science Letters, 333, 101-111.

Lohrmann, J., N. Kukowski, J. Adam, and O. Oncken (2003), The impact of analogue material properties on the geometry, kinematics, and dynamics of convergent sand wedges, J. Struct. Geol., 25, 1691–1711.

Lu, H., Ye, J., Guo, L., Pan, J., Xiong, S., & Li, H. (2019). Towards a clarification of the provenance of Cenozoic sediments in the northeastern Qaidam Basin. Lithosphere, 11(2), 252-272.

Malavieille, J., & Trullenque, G. (2009). Consequences of continental subduction on forearc basin and accretionary wedge deformation in SE Taiwan: insights from analogue modeling. Tectonophysics, 466(3-4), 0-394.

McClay, K. R., and P. S. Whitehouse (2004), Analog modeling of doubly vergent thrust wedges, in Thrust Tectonics and Hydrocarbon Systems, edited by K. R. McClay, AAPG Mem., 82, 184–206.

McClay, K. R., Whitehouse, P. S., Dooley, T., & Richards, M. (2004). 3D evolution of fold and thrust belts formed by oblique convergence. Marine & Petroleum Geology, 21(7), 0-877.

Meng, Q., & Hodgetts, D. (2019). Combined control of décollement layer thickness and cover rock cohesion on structural styles and evolution of fold belts: a discrete element modelling study. Tectonophysics.

Meyer, B., Tapponnier, P., Bourjot, L., Metivier, F., Gaudemer, Y., Peltzer, G., Shunmin, G., & Zhitai, C. (1998). Crustal thickening in Gansu-Qinghai, lithospheric mantle subduction, and oblique, strike-slip controlled growth of the Tibet plateau. Geophysical Journal International, 135(1), 1-47.

Metivier, F., Gaudemer, Y., Tapponnier, P., & Meyer, B. (1998). Northeastward growth of the Tibet plateau deduced from balanced reconstruction of two depositional areas: The Qaidam and Hexi Corridor basins, China. Tectonics, 17(6), 823-842.

Naylor, M., H. D. Sinclair, S. Willett, and P. A. Cowie (2005), A discrete element model for orogenesis and accretionary wedge growth, J. Geophys. Res., 110, B12403, doi:10.1029/2003JB002940.

Naylor, M., & Sinclair, H. D. (2007). Punctuated thrust deformation in the context of doubly vergent thrust wedges: implications for the localization of uplift and exhumation. Geology, 35(6), 559-562.

Nie, J., Ren, X., Saylor, J. E., Su, Q., Horton, B. K., Bush, M. A., ... & Pfaff, K. (2020). Magnetic polarity stratigraphy, provenance, and paleoclimate analysis of Cenozoic strata in the Qaidam Basin, NE Tibetan Plateau. Geological Society of America Bulletin, 310-320.

Pang, J., Yu, J., Zheng, D., Wang, W., Ma, Y., Wang, Y., et al. (2019a). Neogene expansion of the Qilian Shan, north Tibet: Implications for the dynamic evolution of the Tibetan Plateau. Tectonics, 38, 1018–1032. https://doi. org/10.1029/2018TC005258

Pang, J., Yu, J., Zheng, D., Wang, Y., Zhang, H., & Li, C., et al. (2019b). Constraints of new apatite fission-track ages on the tectonic pattern and geomorphic development of the northeastern margin of the tibetan plateau. Journal of Asian Earth Sciences, 181(SEP.1), 103909.1-103909.10.

Persson, K. S. (2001). Effective indenters and the development of double-vergent orogens: Insights from analogue sand models. Geological Society of America Memoirs, 191-206.

Qi, B., Hu, D., Yang, X., Zhang, Y., Tan, C., Zhang, P., & Feng, C. (2016). Apatite fission track evidence for the Cretaceous–Cenozoic cooling history of the Qilian Shan (NW China) and for stepwise northeastward growth of the northeastern Tibetan Plateau since early Eocene. Journal of Asian Earth Sciences, 28-41.

Ramberg, H. (1981), Gravity, deformation, and the Earth's crust, in Theory, Experiments, and Geological Applications, 2nd revised ed., Academic, London.

Reber, J. E., Cooke, M. L., & Dooley, T. P. (2020). What model material to use? A Review on rock analogs for structural geology and tectonics. Earth-Science Reviews, 202. 103107.

Ritter, M. C., K. Leever, M. Rosenau, and O. Oncken (2016), Scaling the sandbox—Mechanical (dis) similarities of granular materials and brittle rock, J. Geophys. Res. Solid Earth, 121, 6863–6879, doi:10.1002/2016JB012915.

Schellart, W.P., 2000. Shear test results for cohesion and friction coefficients for different granular materials: scaling implications for their usage in analogue modelling. Tectonophysics 324, 1–16, http://dx.doi.org/10.1016/S0040-1951(00)00111-6.

Shen, X., Yuan, X., & Liu, M. (2015). Is the Asian lithosphere underthrusting beneath northeastern Tibetan Plateau? Insights from seismic receiver functions. Earth and Planetary Science Letters, 428, 172-180.

Shen, X., Liu, M., Gao, Y., Wang, W., Shi, Y., An, M., ... & Liu, X. (2017). Lithospheric structure across the northeastern margin of the Tibetan Plateau: Implications for the plateau's lateral growth. Earth and Planetary Science Letters, 459, 80-92.

Shi, J., Shi, D., Shen, Y., Zhao, W., Xue, G., & Su, H., et al. (2017). Growth of the northeastern margin of the Tibetan Plateau by squeezing up of the crust at the boundaries. Scientific Reports, 7(1), 10591.

Soto, R., Storti, F., & Casassainz, A. M. (2006). Impact of backstop thickness lateral variations on the tectonic architecture of orogens: Insights from sandbox analogue modeling and application to the Pyrenees. Tectonics, 25(2).

Song, B., Spicer, R. A., Zhang, K., Ji, J., Farnsworth, A., Hughes, A. C., ... & Shi, G. (2020). Qaidam Basin leaf fossils show northeastern Tibet was high, wet and cool in the early Oligocene. Earth and

Planetary Science Letters. 537, 116175.

Song, S., Niu, Y., Su, L., Zhang, C., & Zhang, L. (2014). Continental orogenesis from ocean subduction, continent collision/subduction, to orogen collapse, and orogen recycling: The example of the North Qaidam UHPM belt, NW China. Earth Science Reviews, 129, 59-84.

Storti, F., Salvini, F., & Mcclay, K. (2000). Synchronous and velocity‐partitioned thrusting and thrust polarity reversal in experimentally produced, doubly‐vergent thrust wedges: Implications for natural orogens. Tectonics, 19(2), 378-396.

Storti, F., Marin, R. S., Faccenna, C., & Sainz, A. M. (2001). Role of the backstop-to-cover thickness ratio on vergence partitioning in experimental thrust wedges. Terra Nova, 13(6), 413-417.

Sun, C., et al. (2016), Sandbox modeling of evolving thrust wedges with different preexisting topographic relief: Implications for the Longmen Shan thrust belt, eastern Tibet, J. Geophys. Res. Solid Earth, 121, 4591–4614, doi:10.1002/2016JB013013.

Sun, C., Li, Z., Zheng, W., Jia, D., Zhang, D., Fan, X., & Zhang, P. (2019). 3D geometry of range front blind ramp and its effects on structural segmentation of the southern Longmen Shan front, eastern Tibet. Journal of Asian Earth Sciences.

Sun, M., Yin, A., Yan, D., Ren, H., Mu, H., Zhu, L., & Qiu, L. (2018). Role of pre-existing structures in controlling the Cenozoic tectonic evolution of the eastern Tibetan plateau: New insights from analogue experiments. Earth and Planetary Science Letters, 207-215.

Tapponnier, P., Meyer, B., Avouac, J., Peltzer, G., Gaudemer, Y., Shunmin, G., Hongfa, H. Kelun, Y., Zhitai, C., Shuanhua, Cai., & Huagang, D. (1990). Active thrusting and folding in the Qilian Shan, and decoupling between upper crust and mantle in northeastern Tibet. Earth and Planetary Science Letters, 382-403.

Tapponnier, P., Zhiqin, X., Roger, F., Meyer, B., Arnaud, N., Wittlinger, G., and Jingsui, Y., 2001, Oblique stepwise rise and growth of the Tibet Plateau: Science, v. 294, no. 5547, p. 1671– 1677, doi: 10 .1126 /science .105978

Wang, W. H., & Davis, D. M. (1996). Sandbox model simulation of forearc evolution and noncritical wedges. journal of geophysical research solid earth, 101(B5), 11329-11339.

Wang, W., Zheng, W., Zhang, P., Li, Q., Kirby, E., Yuan, D., ... & Pang, J. (2017). Expansion of the Tibetan Plateau during the Neogene. Nature Communications, 8(1), 1-12.

Wang, W., Zheng, D., Li, C., Wang, Y., Zhang, Z., Pang, J., et al. (2020). Cenozoic exhumation of the Qilian Shan in the northeastern Tibetan Plateau: Evidence from low - temperature thermochronology. Tectonics, 39, e2019TC005705. https:// doi.org/10.1029/2019TC005705

Wei, S. S., Chen, Y. J., Sandvol, E., Zhou, S., Yue, H., Jin, G., ... & Ni, J. (2010). Regional earthquakes in northeastern Tibetan Plateau: Implications for lithospheric strength in Tibet. Geophysical Research Letters, 37(19).

Wei, X., M. Jiang, X. Liang, L. Chen, and Y. Ai (2017), Limited southward underthrusting of the Asian lithosphere and material extrusion beneath the northeastern margin of Tibet, inferred from teleseismic Rayleigh wave tomography, J. Geophys. Res. Solid Earth,122, 7172–7189, doi:10.1002/2016JB013832.

Willett, S., Beaumont, C., & Fullsack, P. (1993). Mechanical model for the tectonics of doubly vergent compressional orogens. Geology, 21(4), 371-374.

Yang, Y., M. H. Ritzwoller, Y. Zheng, W. Shen, A. L. Levshin, and Z. Xie (2012), A synoptic view of the distribution and connectivity of the mid-crustal low velocity zone beneath Tibet, J. Geophys. Res., 117, B04303, doi:10.1029/2011JB008810

Ye, Z., Gao, R., Li, Q., Zhang, H., Shen, X., Liu, X., & Gong, C. (2015). Seismic evidence for the North China plate underthrusting beneath northeastern Tibet and its implications for plateau growth. Earth and Planetary Science Letters, 109-117.

Yin, A., & Harrison, T. M. (2000). Geologic Evolution of the Himalayan-Tibetan Orogen. Annual Review of Earth and Planetary Sciences, 28(1), 211-280.

Yin, A., Rumelhart, P. E., Butler, R. F., Cowgill, E., Harrison, T. M., Foster, D. A., R.V. Ingersoll, Zhang Qing, Zhou Xian-Qiang, Wang Xiao-Feng, A. Hanson & Raza, A. (2002). Tectonic history of the Altyn Tagh fault system in northeastern Tibet inferred from Cenozoic sedimentation. Geological Society of America Bulletin, 114(10), 1257-1295.

Yin, A., Dang, Y. Q., Wang, L. C., Jiang, W. M., Zhou, S. P., Chen, X. H., Gehrels, G. E., & Mcrivette, M. W. (2008a). Cenozoic tectonic evolution of Qaidam basin and its surrounding regions (Part 1): The southern Qilian Shan-Nan Shan thrust belt and northeastern Qaidam basin. Geological Society of America Bulletin, 813-846.

Yin, A., Dang, Y., Zhang, M., Chen, X., & Mcrivette, M. W. (2008b). Cenozoic tectonic evolution of the Qaidam basin and its surrounding regions (Part 3): Structural geology, sedimentation, and regional tectonic reconstruction. Geological Society of America Bulletin, 847-876.

Yu, J., Pang, J., Wang, Y., Zheng, D., Liu, C., Wang, W., ... & Xiao, L. (2019). Mid-Miocene uplift of the northeastern Qilian Shan as a result of the northward growth of the northeastern Tibetan Plateau. Geosphere, 15(2), 423-432.

Yu, X., Guo, Z., Guan, S., Du, W., Wang, Z., Bian, Q., & Li, L. (2019). Landscape and Tectonic Evolution of Bayin River Watershed, Northeastern Qaidam Basin, Northeastern Tibetan Plateau: Implications for the Role of River Morphology in Source Analysis and Low - Temperature

Thermochronology. Journal of Geophysical Research, 124(7), 1701-1719.

Yuan, D. Y., Ge, W. P., Chen, Z. W., Li, C., Wang, Z. C., Zhang, H., ... & Roe, G. H. (2013). The growth of northeastern Tibet and its relevance to large-scale continental geodynamics: A review of recent studies. Tectonics, 32(5), 1358-1370.

Zhao, J., Yuan, X., Liu, H., Kumar, P., Pei, S., & Kind, R., et al. (2010). The boundary between the indian and asian tectonic plates below Tibet. Proceedings of the National Academy of Sciences, 107(25), 11229-11233.

Zhao, W., Kumar, P., Mechie, J., Kind, R., Meissner, R., & Wu, Z., et al. (2011). Tibetan plate overriding the asian plate in central and northeastern tibet. Nature Geoscience, 4(12), 870-873.

Zuza, A. V., Cheng, X., & Yin, A. (2016). Testing models of Tibetan Plateau formation with Cenozoic shortening estimates across the Qilian Shan–Nan Shan thrust belt. Geosphere, 12(2), 501-532.

Zuza, A. V., Wu, C., Wang, Z., Levy, D. A., Li, B., Xiong, X., & Chen, X. (2019). Underthrusting and duplexing beneath the northeastern Tibetan Plateau and the evolution of the Himalayan-Tibetan orogen. Lithosphere, 11(2), 209-231.

Zhang, H., Zhang, P., Prush, V., Zheng, D., Zheng, W., Wang, W., C, Liu., & Ren, Z. (2017). Tectonic geomorphology of the Qilian Shan in the northeastern Tibetan Plateau: Insights into the plateau formation processes. Tectonophysics, 103-115.

Zhang, P. Z., Shen, Z., Wang, M., Gan, W., Bürgmann, R., Molnar, P., ... & Hanrong, S. (2004). Continuous deformation of the Tibetan Plateau from global positioning system data. Geology, 32(9), 809-812.

Zhang, Z., Deng, Y., Teng, J., Wang, C., Gao, R., Chen, Y., & Fan, W. (2011). An overview of the crustal structure of the Tibetan plateau after 35 years of deep seismic soundings. Journal of Asian Earth Sciences, 40(4), 977-989.

Zheng, D. W., M. K. Clark, P. Z. Zhang, W. J. Zheng, and K. A. Farley (2010), Erosion, fault initiation and topographic growth of the North Qilian Shan (northeastern Tibetan Plateau), Geosphere, 6, 937–941.

Zheng, D., Wang, W., Wan, J., Yuan, D., Liu, C., Zheng, W., ... & Zhang, P. (2017). Progressive northward growth of the northeastern Qilian Shan–Hexi Corridor (northeastern Tibet) during the Cenozoic. Lithosphere, 9(3), 408-416.

Zheng, W. J., P. Z. Zhang, W. P. Ge, P. Molnar, H. P. Zhang, D. Y. Yuan, and J. H. Liu (2013), Late Quaternary slip rate of the South Heli Shan Fault (northeastern Hexi Corridor, NW China) and its implications for northeastward growth of the Tibetan Plateau, Tectonics, 32, 271–293,

doi:10.1002/tect.20022.

Zhuang, G., Johnstone, S. A., Hourigan, J. K., Ritts, B. D., Robinson, A. C., & Sobel, E. R. (2018). Understanding the geologic evolution of Northeastern Tibetan Plateau with multiple thermochronometers. Gondwana Research, 195-210.